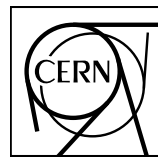


EUROPEAN ORGANIZATION FOR NUCLEAR RESEARCH



CERN-PH-EP-2015-136

03 Jun 2015

Measurement of jet quenching with semi-inclusive hadron-jet distributions in central Pb–Pb collisions at $\sqrt{s_{\text{NN}}} = 2.76$ TeV

ALICE Collaboration*

Abstract

We report the measurement of a new observable of jet quenching in central Pb–Pb collisions at $\sqrt{s_{\text{NN}}} = 2.76$ TeV, based on the semi-inclusive rate of charged jets recoiling from a high transverse momentum (high- p_T) charged hadron trigger. Jets are measured using collinear-safe jet reconstruction with infrared cutoff for jet constituents of 0.15 GeV/ c , for jet resolution parameters $R = 0.2, 0.4$ and 0.5 . Underlying event background is corrected at the event-ensemble level, without imposing bias on the jet population. Recoil jet spectra are reported in the range $20 < p_{\text{T},\text{jet}}^{\text{ch}} < 100$ GeV/ c . Reference distributions for pp collisions at $\sqrt{s} = 2.76$ TeV are calculated using Monte Carlo and NLO pQCD methods, which are validated by comparing with measurements in pp collisions at $\sqrt{s} = 7$ TeV. The recoil jet yield in central Pb–Pb collisions is found to be suppressed relative to that in pp collisions. No significant medium-induced broadening of the intra-jet energy profile is observed within 0.5 radians relative to the recoil jet axis. The angular distribution of the recoil jet yield relative to the trigger axis is found to be similar in central Pb–Pb and pp collisions, with no significant medium-induced acoplanarity observed. Large-angle jet deflection, which may provide a direct probe of the nature of the quasi-particles in hot QCD matter, is explored.

© 2015 CERN for the benefit of the ALICE Collaboration.

Reproduction of this article or parts of it is allowed as specified in the CC-BY-4.0 license.

*See Appendix A for the list of collaboration members

1 Introduction

Hadronic jets are unique probes of the hot Quantum Chromodynamic (QCD) matter generated in nuclear collisions at collider energies. Interactions of hard-scattered partons with colored matter may modify intra-jet structure, softening and broadening the distribution of hadronic jet fragments relative to jets generated in vacuum, and may deflect jets by large angles. These phenomena, known as jet quenching [1], can probe dynamical properties of the hot QCD medium [2] and the nature of quasi-particles in the Quark-Gluon Plasma (QGP) [3].

Jet quenching generates marked, experimentally observable effects. Measurements of inclusive distributions and correlations of high transverse momentum (high- p_T) hadrons have revealed significant yield suppression in nuclear collisions relative to vacuum [4–16]. Suppression of the inclusive yield of reconstructed jets [17–20] and enhancement in the rate of energy-imbalanced back-to-back di-jet pairs [21, 22] have also been observed in nuclear collisions. A measurement of event-averaged missing p_T suggests that the radiated energy induced by the interaction of an energetic parton with the medium is carried to a significant extent by soft particles at large angles relative to the jet axis [23].

The measurement of reconstructed jets over a wide range in jet energy and jet resolution parameter (R) is required for comprehensive understanding of jet quenching in heavy-ion collisions. Such measurements are challenging, however, due to the presence of complex, uncorrelated background to the jet signal, and the need to minimize biases in the selected jet population imposed by background suppression techniques. Multiple, complementary measurement approaches, differing both in instrumentation and in analysis algorithm, are therefore important to elucidate the physics of jet quenching using reconstructed jets.

In this article we present a new approach to the measurement of jet quenching, based on the semi-inclusive distribution of charged jets recoiling from a high- p_T charged hadron trigger (“h-jet” coincidence) in central (0–10%) Pb–Pb collisions at $\sqrt{s_{\text{NN}}} = 2.76$ TeV. Jets are reconstructed using charged particle tracks with the k_T [24] and anti- k_T algorithms [25], with infrared cutoff for tracks $p_{T,\text{const}} > 0.15$ GeV/c. Uncorrelated background to the recoil jet signal is corrected solely at the level of ensemble-averaged distributions, without event-by-event discrimination of jet signal from background, using a technique that exploits the phenomenology of jet production in QCD. The correction is carried out using an unfolding technique. This approach enables the collinear-safe measurement in heavy-ion collisions of reconstructed jets with low infrared cutoff over a wide range of jet energy and R . Recoil jet distributions, which are differential in $p_{T,\text{jet}}$ and in azimuthal angle relative to the trigger axis, are reported for $R = 0.2$, 0.4 and 0.5, over the range $20 < p_{T,\text{jet}}^{\text{ch}} < 100$ GeV/c.

Suppression of the recoil jet yield due to quenching is measured by comparison to the yield in pp collisions. However, our current data for pp collisions at $\sqrt{s} = 2.76$ TeV do not have sufficient statistical precision to provide a reference for the Pb–Pb measurements reported here. The reference distribution is therefore calculated using the PYTHIA event generator [26] and perturbative QCD (pQCD) calculations at Next-to-Leading Order (NLO) [27], which are validated by comparison with ALICE measurements of pp collisions at $\sqrt{s} = 7$ TeV. Angular broadening of the internal jet structure due to quenching is investigated by comparing the differential recoil jet distributions for different values of R . Acoplanarity between the trigger hadron and recoil jet directions is measured to explore the deflection of the jet axis induced by quenching. The rate of large angular deviations is measured; this rate may be dominated by single hard (Molière) scattering, which could potentially probe the quasi-particle nature of the hot QCD medium [3, 28].

These observables are directly comparable to theoretical calculations, without the need to model the heavy-ion collision background, due to utilization of a hadron trigger, the semi-inclusive nature of the observables, and the background suppression technique. The only non-perturbative component required to calculate the hard-process bias is the inclusive charged hadron fragmentation function (in-vacuum or

quenched) for the trigger hadron.

The paper is organized as follows: Sect. 2, dataset, event selection, and simulations; Sect. 3, jet reconstruction; Sect. 4, discussion of observables; Sect. 5, raw distributions; Sect. 6, corrections; Sect. 7, systematic uncertainties; Sect. 8, reference distributions for pp collisions; Sect. 9, results; and Sect. 10, summary.

2 Data set, offline event selection, and simulations

The ALICE detector and its performance are described in [29, 30].

The Pb–Pb collision data were recorded during the 2011 LHC Pb–Pb run at $\sqrt{s_{\text{NN}}} = 2.76$ TeV. This analysis uses the 0–10% most-central Pb–Pb collisions selected by the online trigger based on the hit multiplicity measured in the forward V0 detectors. The online trigger had 100% efficiency for the 0–7% interval in centrality percentile, and 80% efficiency for the 8–10% interval.

Events are reconstructed offline as described in Ref. [13]. Charged tracks are measured in the ALICE central barrel, with acceptance $|\eta| < 0.9$ over the full azimuth. Accepted tracks are required to have $0.15 < p_{\text{T}} < 100$ GeV/ c , with at least 70 Time Projection Chamber (TPC) space-points and at least 80% of the geometrically findable space-points in the TPC. To account for the azimuthally non-uniform response of the Inner Tracking System (ITS) in this dataset, two exclusive classes of tracks are used [30]: tracks with Silicon Pixel Detector (SPD) hits (70% of all tracks in central Pb–Pb collisions, and 95% in pp collisions); and tracks without SPD hits but with a primary vertex constraint. The primary vertex is required to lie within 10 cm of the nominal center of the detector along the beam axis, and within 1 cm of it in the transverse plane. After offline event selection, the Pb–Pb dataset consists of 17M events in the 0–10% centrality percentile interval.

The pp collision data used to validate PYTHIA and pQCD calculations were recorded during the 2010 low-luminosity pp run at $\sqrt{s} = 7$ TeV, using a MB trigger. The MB trigger configuration, offline event selection, and tracking are the same as described in [31]. After event selection cuts, the pp dataset consists of 168M events. There is negligible difference in the inclusive jet cross section for events selected by the ALICE online trigger, and for a non-single diffractive event population.

Simulations of pp collisions were carried out using PYTHIA 6.425, with the Perugia 0, Perugia 2010, and Perugia 2011 tunes [32]. Instrumental effects are calculated using the Perugia 0 and Perugia 2010 tunes for pp and Pb–Pb collisions respectively, with a detailed detector model implemented using GEANT3 [33]. In addition, a simulation based on HIJING [34] is used to evaluate the detector response in the high multiplicity environment of Pb–Pb collisions. Perugia 2011, which has been tuned to other LHC data, is used as an alternative to compare with the new data presented here. Simulated events, which include primary particles and the daughters of strong and electromagnetic decays but not instrumental effects or the daughters of weak decays, are denoted “particle level”. Simulated events also including instrumental effects and weak decay daughters where reconstructed tracks are selected using the experimental cuts are denoted “detector level”.

For central Pb–Pb collisions, tracking efficiency is 80% for $p_{\text{T}} > 1$ GeV/ c , decreasing to 56% at 0.15 GeV/ c . Track momentum resolution is 1% at $p_{\text{T}} = 1$ GeV/ c and 3% at $p_{\text{T}} = 50$ GeV/ c . For pp collisions, tracking efficiency is 2%–3% higher than in central Pb–Pb collisions. Track momentum resolution is 1% at $p_{\text{T}} = 1$ GeV/ c for all reconstructed tracks; 4% at $p_{\text{T}} = 40$ GeV/ c for tracks with SPD hits; and 7% at $p_{\text{T}} = 40$ GeV/ c for tracks without SPD hits [30, 31].

3 Jet reconstruction

Jet reconstruction for both the pp and Pb–Pb analyses is carried out using the k_T [24] and anti- k_T [25] algorithms applied to all accepted charged tracks. The boost-invariant p_T -recombination scheme is used [24]. Jet area is calculated by the Fastjet algorithm using ghost particles with area 0.005 [35].

Charged jets are not safe in perturbation theory, because radiation carried by neutral particles is not included. However, infrared-safe calculations of charged-jet observables can be performed using non-perturbative track functions, which absorb infrared divergences and describe the energy fraction of a parton carried by charged tracks [36]. Track functions are analogous to fragmentation functions, with DGLAP-like evolution, and perturbative calculations using them are in good agreement with PYTHIA calculations [36]. Track functions can provide the basis for rigorous comparison of the charged-jet measurements reported here with both analytic and Monte Carlo QCD calculations.

For the Pb–Pb analysis, adjustment of jet energy for the presence of large background utilizes the FastJet procedure [37], in which jet reconstruction is carried out twice for each event. The first pass applies the k_T algorithm with $R = 0.4$ to estimate ρ , the density of jet-like transverse-momentum due to background, which is defined as

$$\rho = \text{median} \left\{ \frac{p_{T,\text{jet}}^{\text{raw},i}}{A_{\text{jet}}^i} \right\}, \quad (1)$$

where index i runs over all jet candidates in an event, and $p_{T,\text{jet}}^{\text{raw},i}$ and A_{jet}^i are the transverse momentum and area of the i^{th} reconstructed jet. Further details are presented in [38]. The central data points in this analysis are determined by excluding the two jets with highest $p_{T,\text{jet}}^{\text{raw},i}$ from calculation of the median, with a variant used to study systematic sensitivity to this choice.

The second pass, which generates jet candidates for the reported distributions, applies the anti- k_T algorithm with resolution parameter $R = 0.2, 0.4$, and 0.5 . The value of $p_{T,\text{jet}}^{\text{raw},i}$ is corrected according to [37],

$$p_{T,\text{jet}}^{\text{reco},i} = p_{T,\text{jet}}^{\text{raw},i} - \rho \cdot A_{\text{jet}}^i, \quad (2)$$

where $p_{T,\text{jet}}^{\text{raw},i}$ and A_{jet}^i are measured for the i^{th} jet in an event, and ρ is a scalar value common to all jets in each event, but varies from event to event.

Jet candidates are accepted if $|\eta_{\text{jet}}| < 0.5$ for $R = 0.2$ and 0.4 and $|\eta_{\text{jet}}| < 0.4$ for $R = 0.5$, where η_{jet} is the pseudo-rapidity of the jet candidate centroid. The azimuthal acceptance of the recoil yield measurement is $\pi - \Delta\varphi < 0.6$, where $\Delta\varphi = |\varphi_{\text{trig}} - \varphi_{\text{jet}}|$ is the difference between the azimuthal angle of the trigger hadron (φ_{trig}) and the jet candidate centroid (φ_{jet}), and $0 \leq \Delta\varphi \leq \pi$.

A cut on jet area is applied to suppress combinatorial jets while preserving high efficiency for true hard jets [39, 40]. Jet candidates are rejected if $A_{\text{jet}}^i < 0.07$ for $R = 0.2$; $A_{\text{jet}}^i < 0.4$ for $R = 0.4$; and $A_{\text{jet}}^i < 0.6$ for $R = 0.5$.

Similar procedures are followed for the pp data analysis. Jets are reconstructed with the anti- k_T algorithm for $R = 0.2, 0.4$ and 0.5 . Reconstructed $p_{T,\text{jet}}^{\text{reco},\text{ch}}$ is adjusted using Eq. 2, where ρ is estimated in this case by the summed p_T in two cones of radius $R = 0.4$, with centroids at the same η but perpendicular in azimuth to the leading jet in the event.

The instrumental jet energy resolution (JER), which characterizes the detector response relative to charged jets at the particle level, varies from 20% at $p_{T,\text{jet}} = 20 \text{ GeV}/c$ to 25% at $p_{T,\text{jet}} = 100 \text{ GeV}/c$, for both Pb–Pb and pp collisions, with negligible dependence on R . The jet energy scale (JES) uncertainty, which

is dominated by the uncertainty of tracking efficiency, is approximately 5% for both Pb–Pb and pp collisions, with negligible dependence on $p_{T,\text{jet}}^{\text{ch}}$ and R . However, the instrumental response is significantly non-Gaussian [17] and unfolding of the full response matrix is used for corrections.

4 Discussion of observables

4.1 General considerations

Energetic jets that arise from high momentum transfer (high- Q^2) scattering of partons are readily visible in event displays of high multiplicity heavy-ion collisions [22, 23]. However, accurate measurement of jet energy in such events, and unbiased measurement of jet distributions, are more difficult. Application of a jet reconstruction algorithm to high multiplicity events will cluster hadrons arising from multiple incoherent sources into each reconstructed jet, resulting in significant smearing of the true hard jet energy distribution. It will also generate a large population of “combinatorial” background jets comprising solely hadrons generated by soft production processes (Q^2 below a few GeV 2), which cannot be identified as hard jets with smeared energy.

Current heavy-ion jet analyses select the hard jet population on a jet-by-jet basis by several different approaches: removal of an estimated background component of transverse energy prior to jet reconstruction [41]; or imposition of a fragmentation bias requiring a cluster of high- p_T tracks or a single high- p_T track in the jet, and imposition of a jet p_T threshold [17, 19, 20, 42]. These rejection techniques may bias towards certain fragmentation patterns in the accepted hard jet population.

This analysis takes a different approach, in which corrections for background and instrumental effects are applied solely at the level of ensemble-averaged distributions, without rejection of individual jet candidates or removal of event components. The analysis is based on the semi-inclusive differential distribution of charged jets recoiling from a high- p_T trigger hadron, with the trigger hadron selected within a limited $p_{T,\text{trig}}$ interval (Trigger Track, or TT, class). This distribution, which is the number of jets measured in the recoil acceptance normalized by the number of trigger hadrons, is equivalent to the ratio of inclusive production cross sections,

$$\frac{1}{N_{\text{trig}}^{\text{AA}}} \frac{d^2N_{\text{jet}}^{\text{AA}}}{dp_{T,\text{jet}}^{\text{ch}} d\eta_{\text{jet}}} \bigg|_{p_{T,\text{trig}} \in \text{TT}} = \left(\frac{1}{\sigma^{\text{AA} \rightarrow h+X}} \cdot \frac{d^2\sigma^{\text{AA} \rightarrow h+\text{jet}+X}}{dp_{T,\text{jet}}^{\text{ch}} d\eta_{\text{jet}}} \right) \bigg|_{p_{T,h} \in \text{TT}}, \quad (3)$$

where AA denotes pp or Pb–Pb collisions, $\sigma^{\text{AA} \rightarrow h+X}$ is the cross section to generate a hadron within the p_T interval of the selected TT class, $d^2\sigma^{\text{AA} \rightarrow h+\text{jet}+X}/dp_{T,\text{jet}}^{\text{ch}} d\eta$ is the differential cross section for coincidence production of a hadron in the TT interval and a recoil jet, and $p_{T,\text{jet}}^{\text{ch}}$ and η_{jet} are the charged jet transverse momentum and pseudo-rapidity.

Because the observable in Eq. 3 is semi-inclusive, the selection of events containing a hard process (“hard-process selection”) is based solely on the presence of a high- p_T hadron trigger. In particular, there is no requirement that a jet satisfying certain criteria be found in the recoil acceptance. Rather, all jet candidates in the recoil acceptance are counted in Eq. 3, regardless of their specific properties. Events with no hard jet candidates (however defined) falling within the acceptance are not rejected, and contribute to the normalization. This observable thereby measures the absolutely normalized rate of recoil jets observed per trigger. Correction for the contribution of uncorrelated background jets in Eq. 3 is carried out at a later step in the analysis, as discussed below.

Other jet correlation measurements in heavy-ion collisions have been carried out, in which hard-process selection utilizes a compound condition that requires the presence of both a trigger object (jet or photon) and a recoil jet satisfying certain criteria [22, 23, 43]. The jet correlation distributions in these analyses

are normalized per trigger–recoil pair; absolute normalization requires scaling by the inclusive trigger yield, together with selection of the recoil jet population using the semi-inclusive procedure described above. The role of normalization in the measurement of in-medium large-angle scattering is discussed in Sect. 9.2.

4.2 Trigger hadrons and hard-process bias

The use of high- p_T hadron triggers for hard-process selection in this analysis is based on the following considerations.

Hadrons with p_T larger than about 5–7 GeV/ c are expected to originate primarily from fragmentation of energetic jets, in both pp and Pb–Pb collisions at $\sqrt{s_{\text{NN}}} = 2.76$ TeV (see e.g. [44]). They provide experimentally clean triggers, without the need for correction for uncorrelated background. Selection of events by requiring the presence of a high- p_T hadron biases towards events containing a high- Q^2 partonic interaction, with jets in the final state.

Inclusive distributions of high- p_T hadrons have been measured and calculated theoretically in both pp and heavy-ion collisions at collider energies. For pp collisions at the LHC, agreement within a factor two is found between NLO calculations and data for $p_T > 10$ GeV/ c , with the discrepancies attributable to poorly constrained gluon fragmentation functions that can be improved by fitting to LHC data [45]. For inclusive hadron production in heavy-ion collisions [5, 9, 13, 14], the medium-induced modification and evolution of fragmentation functions have been calculated in several frameworks, showing good agreement with data ([46, 47] and references therein). Suppression of inclusive hadron production in heavy-ion collisions has been used to determine the jet transport parameter \hat{q} [2].

Any hard-process selection procedure imposes bias on the accepted event population, and accurate comparison of theory calculations with such measurements requires calculation of this selection bias. In this analysis, hard-process selection uses the same cuts as those used for high- p_T inclusive hadron measurements. Since inclusive hadron production is calculable in both pp and Pb–Pb collisions, the selection bias in this analysis is likewise calculable using current theoretical approaches.

4.3 Hadron–jet coincidences

There are additional considerations for interpreting hadron-triggered recoil distributions in Eq. 3 and comparing such measurements to theoretical calculations, as follows.

The h-jet coincidence cross section in pp collisions has been calculated in a pQCD framework [27]. In this process at LO, a pair of final-state partons is generated with opposing transverse momenta, with one of the pair fragmenting into a hadron which carries momentum fraction z of the recoiling jet. Since $z = p_{T,\text{trig}}/p_{T,\text{jet}} \leq 1$ at LO, the requirement of a high- $p_{T,\text{trig}}$ hadron above threshold therefore biases against coincident recoil jets with $p_{T,\text{jet}} < p_{T,\text{trig}}$, but does not impose a kinematic constraint on recoil jets with $p_{T,\text{jet}} > p_{T,\text{trig}}$.

The inclusive hadron distribution at high- p_T is biased towards high- z jet fragments, due to interplay between the shape of the inclusive jet p_T spectrum and the shape of the inclusive fragmentation function, with $\langle z_{\text{incl}} \rangle \approx 0.6$ at LHC energies [48]. However, in the semi-inclusive measurement based on Eq. 3, the trigger-normalized rate of recoil jets is measured as a function of $p_{T,\text{jet}}^{\text{ch}}$. At LO this corresponds to $z = p_{T,\text{trig}}/p_{T,\text{jet}}$, which can differ significantly from $\langle z_{\text{incl}} \rangle$ [27]. For fixed $p_{T,\text{trig}}$ the z -bias therefore varies as a function of recoil $p_{T,\text{jet}}$, with stronger bias than the inclusive case for $p_{T,\text{jet}} \approx p_{T,\text{trig}}$, and weaker bias for $p_{T,\text{jet}} \gg p_{T,\text{trig}}$. The z -bias has been calculated for pp collisions at $\sqrt{s} = 2.76$ and 7 TeV using the approach of [27] and found to be similar at LO and NLO. This z -bias, which is kinematic in origin, likewise occurs in nuclear collisions in which jets experience quenching. This effect is intrinsic to any theoretical framework based on pQCD, both in-vacuum and quenched, and will be properly accounted for in such calculations.

For quenched jets in nuclear collisions, high- p_T hadron selection may generate two additional, related biases. The first is a bias towards high- z fragments of jets that have lost relatively little energy in the medium [49]. The second is a geometric bias in which small energy loss corresponds to small path length in matter. In the latter case, jets generating high- p_T trigger hadrons are generated predominantly on the surface of the collision region and headed outward [50–56], with the corresponding recoil jet population biased towards longer path length in matter than the unbiased, fully inclusive jet population.

The degree to which high- p_T hadron selection biases towards small energy loss of its parent jet determines the degree of similarity in the underlying distribution of high- Q^2 processes in pp and Pb–Pb collisions, for the same hadron trigger cuts. In the following, we refer to potential differences in such Q^2 distributions as being due to “trigger-jet” energy loss. Quantitative assessment of these effects can be carried out using theoretical calculations of inclusive charged hadron production.

4.4 Semi-inclusive recoil jet measurements

Trigger hadrons lie within the charged-track acceptance $|\eta| < 0.9$ and are selected in the intervals $8 < p_{T,\text{trig}} < 9 \text{ GeV}/c$, denoted by TT{8,9} and referred to as the Reference TT class; and $20 < p_{T,\text{trig}} < 50 \text{ GeV}/c$, denoted by TT{20,50} and referred to as the Signal TT class.

Figure 1 shows semi-inclusive distributions (Eq. 3) for recoil jets with $R = 0.4$, for the Signal and Reference TT classes in pp collisions at $\sqrt{s_{\text{NN}}} = 7 \text{ TeV}$ and central Pb–Pb collisions measured by ALICE, and in pp collisions at $\sqrt{s_{\text{NN}}} = 2.76 \text{ TeV}$ simulated by PYTHIA. The distributions include all jet candidates in the recoil acceptance.

Since ρ is the median energy density in an event, there must be jet candidates with energy density less than ρ , and which consequently have $p_{T,\text{jet}}^{\text{reco},\text{ch}} < 0$. The recoil jet distribution in the region $p_{T,\text{jet}}^{\text{reco},\text{ch}} < 0$ is seen to be largely uncorrelated with TT class in all cases, indicating that the yield in this region is dominated by combinatorial jets. In pp collisions the distribution in this region is narrow, indicating only small background density fluctuations. The predominant feature of the pp distributions is the strong dependence on TT class for $p_{T,\text{jet}}^{\text{reco},\text{ch}} > 0$, with a harder recoil jet spectrum for higher $p_{T,\text{trig}}$, as expected from the systematics of jet production in QCD. For Pb–Pb collisions the distribution in the region $p_{T,\text{jet}}^{\text{reco},\text{ch}} < 0$ is much broader, indicating significantly larger background density fluctuations than in pp collisions. For large and positive $p_{T,\text{jet}}^{\text{reco},\text{ch}}$, the recoil jet distribution in Pb–Pb is strongly correlated with TT class, similar to pp collisions, showing that this region has significant contribution from the true coincident recoil jet yield.

The integrals of the Pb–Pb distributions in Fig. 1 are $1.645 \pm 0.005(\text{stat})$ for TT{8,9} and $1.647 \pm 0.009(\text{stat})$ for TT{20,50}. This integral represents the average number of jet candidates per trigger hadron, both correlated and uncorrelated, and is seen to be consistent, within errors of a few per mil, for the two TT classes. Similar features have been observed in model calculations [57]. Since central Pb–Pb events have high multiplicity, the recoil acceptance in each event is fully populated by jet candidates. Invariance of the integral with TT class therefore indicates that the number of jet candidates per trigger hadron is due largely to geometric factors, specifically the acceptance and jet resolution parameter R . This behavior is consistent with the robustness of the anti- k_T algorithm against modification of jet structure by soft particles from the underlying event [25]. Jet candidate distributions reconstructed using the anti- k_T algorithm for different trigger hadron kinematics appear to differ most significantly in the shape of the distribution as a function of $p_{T,\text{jet}}^{\text{ch}}$, not in the total number of jet candidates per event.

Based on these considerations we define a new observable, Δ_{recoil} , which suppresses the uncorrelated jet yield in a purely data-driven way. Δ_{recoil} is the difference between two semi-inclusive recoil jet distributions (Eq. 3) for the Signal and Reference TT classes [57],

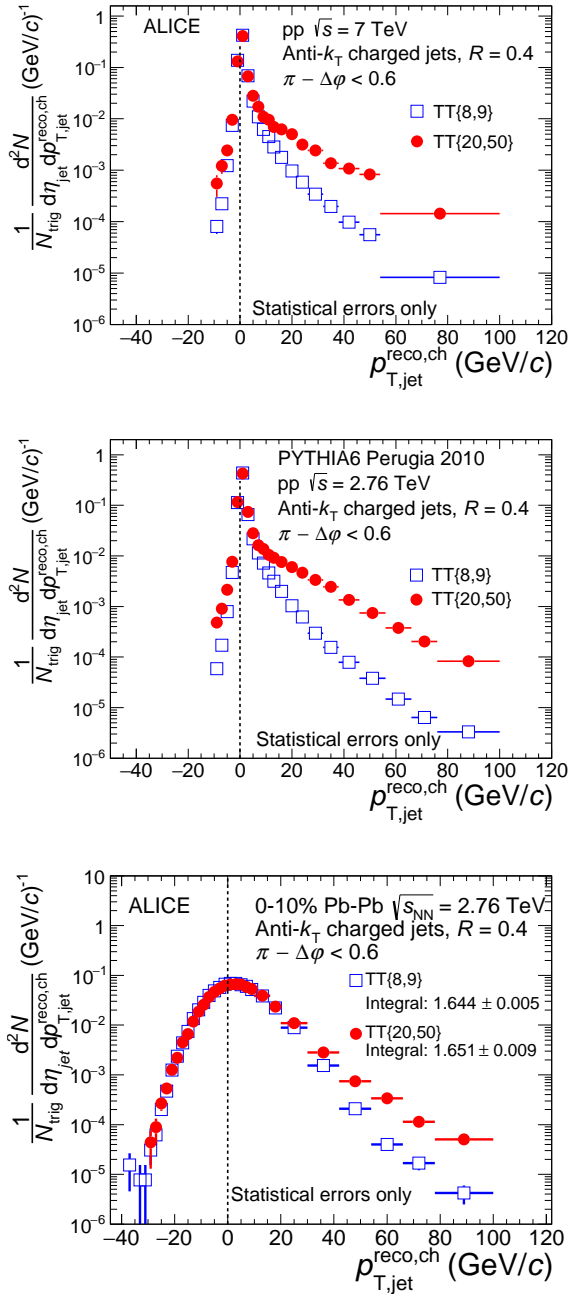


Fig. 1: Semi-inclusive distributions of jets recoiling from a hadron trigger for two exclusive TT classes (Eq. 3), for pp collisions at $\sqrt{s} = 7$ TeV from ALICE data (top), pp collisions at $\sqrt{s} = 2.76$ TeV from particle-level PYTHIA simulations (center), and central Pb–Pb collisions at $\sqrt{s_{NN}} = 2.76$ TeV from ALICE data (bottom). All distributions are a function of $p_{T,\text{jet}}^{\text{reco},\text{ch}}$ (Eq. 2). Distributions from data are not corrected for background fluctuations and instrumental effects.

$$\Delta_{\text{recoil}} = \frac{1}{N_{\text{trig}}^{\text{AA}}} \frac{d^2N_{\text{jet}}^{\text{AA}}}{dp_{T,\text{jet}}^{\text{ch}} d\eta_{\text{jet}}} \Bigg|_{p_{T,\text{trig}} \in \text{TT}_{\text{Sig}}} - c_{\text{Ref}} \cdot \frac{1}{N_{\text{trig}}^{\text{AA}}} \frac{d^2N_{\text{jet}}^{\text{AA}}}{dp_{T,\text{jet}}^{\text{ch}} d\eta_{\text{jet}}} \Bigg|_{p_{T,\text{trig}} \in \text{TT}_{\text{Ref}}} . \quad (4)$$

The scale factor c_{Ref} , which is within a few percent of unity, is discussed in Sect. 5.1.

The raw Δ_{recoil} distribution must be corrected for instrumental effects and for smearing of coincident

recoil jet energy by fluctuations of energy density in the underlying event. After corrections, Δ_{recoil} represents the change in the distribution of jets recoiling in coincidence with a trigger hadron, as the trigger hadron p_{T} changes from the Reference to Signal TT interval. While this differential coincidence observable has not been reported previously, it is nevertheless well-defined in terms of perturbative QCD.

We also extend Eq. 4 to measure the angular distribution of recoil jet yield with respect to the axis defined by the trigger hadron momentum, in order to investigate medium-induced acoplanarity [3, 28] (“inter-jet broadening”). The azimuthal correlation between the trigger hadron and coincident recoil charged jets is measured via

$$\Phi(\Delta\varphi) = \frac{1}{N_{\text{trig}}^{\text{AA}}} \frac{d^2N_{\text{jet}}}{dp_{\text{T},\text{jet}}^{\text{ch}} d\Delta\varphi} \Bigg|_{p_{\text{T},\text{trig}} \in \text{TT}_{\text{Sig}}} - c_{\text{Ref}} \cdot \frac{1}{N_{\text{trig}}^{\text{AA}}} \frac{d^2N_{\text{jet}}}{dp_{\text{T},\text{jet}}^{\text{ch}} d\Delta\varphi} \Bigg|_{p_{\text{T},\text{trig}} \in \text{TT}_{\text{Ref}}}, \quad (5)$$

where the recoil acceptance for this observable is $\pi/2 < \Delta\varphi < \pi$. Normalization to unit η is omitted from the notation for clarity.

We quantify the rate of medium-induced large-angle scattering by measuring the integrated recoil yield at large angular deflection relative to $\Delta\varphi = \pi$, defined as

$$\Sigma(\Delta\varphi_{\text{thresh}}) = \int_{\pi/2}^{\pi - \Delta\varphi_{\text{thresh}}} d\Delta\varphi [\Phi(\Delta\varphi)], \quad (6)$$

where the lower limit of the integration is set arbitrarily to $\pi/2$. The upper limit excludes the main peak of the $\Phi(\Delta\varphi)$ distribution, $|\Delta\varphi - \pi| < \Delta\varphi_{\text{thresh}}$, in order to measure the yield in the tail of the distribution. $\Sigma(\Delta\varphi_{\text{thresh}})$ is measured as a function of $\Delta\varphi_{\text{thresh}}$.

The distributions $\Phi(\Delta\varphi)$ and $\Sigma(\Delta\varphi_{\text{thresh}})$ likewise represent the change in the angular distribution of recoil jet yield, as the trigger hadron p_{T} changes from the Reference to Signal TT interval.

5 Raw distributions

In order to ensure statistical independence of the recoil jet distributions for the Signal and Reference TT classes, each event is assigned randomly to one of the TT classes and is used only for its assigned TT class. The statistical reach of the analysis is optimized by assigning 80% of the events to the Signal TT subset and 20% to the Reference TT subset. This choice balances retention of the high- $p_{\text{T},\text{jet}}^{\text{reco},\text{ch}}$ component of the Signal recoil jet distribution with statistical precision of the Reference distribution in the region $p_{\text{T},\text{jet}}^{\text{reco},\text{ch}} < 0$, with the latter condition required to provide accurate normalization of the combinatorial background jet distribution.

Events within each subset are then selected for further analysis if they contain at least one hadron within the $p_{\text{T},\text{trig}}$ interval of their assigned TT class. If more than one hadron satisfying this criterion is found, one hadron is chosen randomly as the trigger hadron. For the Pb–Pb analysis there are 65k events with trigger hadrons in the Reference TT class and 22k in the Signal TT class. For the pp analysis there are 74k events with trigger hadrons in the Reference TT class and 5k in the Signal TT class.

5.1 Distributions of Δ_{recoil}

Figure 2, left panels, show uncorrected trigger-normalized recoil jet distributions for $R = 0.2, 0.4$ and 0.5 for both Signal and Reference TT classes. The right panels show the ratio of Signal and Reference distributions for each value of R . The error bars in Fig. 2 are statistical only, and are dominated by the statistics of the recoil jet yield in all cases. The statistical error due to trigger hadron yield is negligible.

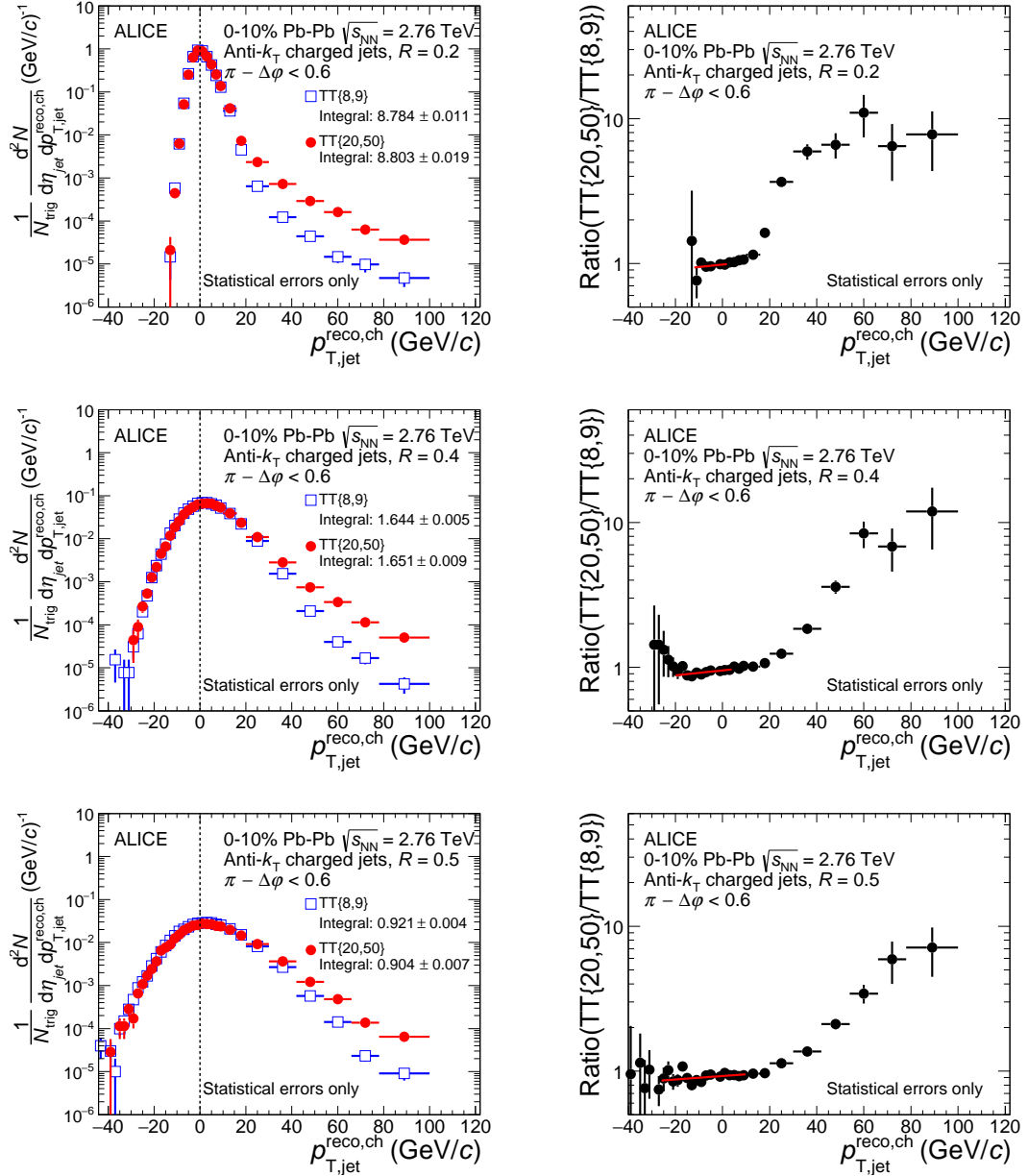


Fig. 2: Uncorrected trigger-normalized recoil charged jet distributions for central Pb–Pb collisions, with Signal TT{20,50} and Reference TT{8,9}. Jets are reconstructed with the anti- k_T algorithm, constituent $p_{T,\text{const}} > 0.15 \text{ GeV}/c$, and $R = 0.2, 0.4$, and 0.5 . Left: individual spectra. Right: their ratios. The red line shows a linear fit in the indicated region. Error bars show statistical errors only. Left-middle panel ($R = 0.4$) is identical to right panel in Fig. 1.

Figure 2, left panels, also show the integrals of the distributions. The integrals are seen to be insensitive to TT class for a given R , with variations at the percent level or smaller, while the value of the integral depends strongly on R . These features are consistent with the geometric interpretation of the integral given in Sect. 4.4.

Table 1 shows the parameters resulting from the fit of a linear function to the ratios in the right panels of Fig. 2, in the region of $p_{T,\text{jet}}^{\text{recoc},\text{ch}}$ where the distributions are largely uncorrelated with TT class. The

R	$p_{T,\text{jet}}^{\text{reco},\text{ch}}$ fit range (GeV/ c)	Constant (c_{Ref} in Eq. 4)	Slope (GeV/ c) $^{-1}$
0.2	[-12, 2]	0.99 ± 0.01	0.004 ± 0.002
0.4	[-20, 4]	0.96 ± 0.01	0.004 ± 0.001
0.5	[-26, 10]	0.93 ± 0.01	0.002 ± 0.001

Table 1: Parameters from linear fits to ratios shown in right panels of Fig. 2.

constant term of the fit, c_{Ref} , is less than unity by a few percent, while the slopes exceed zero by about 2σ . The individual distributions vary by three orders of magnitude in this region.

A value of c_{Ref} below unity arises because the higher TT class has a larger rate of true coincident recoil jets, and the integrals of the distributions are largely uncorrelated with TT class. Larger yield at positive $p_{T,\text{jet}}^{\text{reco},\text{ch}}$ consequently depletes the yield at negative and small positive values of $p_{T,\text{jet}}^{\text{reco},\text{ch}}$.

Accurate subtraction of the uncorrelated component from the Signal TT distribution therefore requires scaling of the Reference TT distribution by c_{Ref} , as indicated in Eq. 4 and Eq. 5. Scaling of the Reference TT distributions in the pp analysis by c_{Ref} has negligible effect.

Figure 3 shows Δ_{recoil} distributions for $R = 0.2, 0.4$ and 0.5 . The left panels, which have linear vertical scale, show Δ_{recoil} in the region of $p_{T,\text{jet}}^{\text{reco},\text{ch}}$ in which the scale factor c_{Ref} is determined. Δ_{recoil} is seen to be consistent with zero over the entire fitting range. These panels also show the close similarity of the shapes of the Signal and Reference distributions in this region.

Figure 3, right panels, show Δ_{recoil} at positive $p_{T,\text{jet}}^{\text{reco},\text{ch}}$, where the Signal and Reference distributions diverge. This is the ensemble-averaged distribution of the trigger-correlated differential jet yield, but with measured $p_{T,\text{jet}}^{\text{reco},\text{ch}}$ not yet corrected for instrumental effects and fluctuations of the underlying event background.

5.2 $\Phi(\Delta\phi)$ and $\Sigma(\Delta\phi_{\text{thresh}})$

The analysis of $\Phi(\Delta\phi)$ (Eq. 5) and $\Sigma(\Delta\phi_{\text{thresh}})$ (Eq. 6) is the same as that for Δ_{recoil} in terms of event selection, track cuts, jet reconstruction, and jet candidate selection. For this analysis we only consider jets with $R = 0.4$ and $40 < p_{T,\text{jet}}^{\text{reco},\text{ch}} < 60$ GeV/ c .

Figure 4, left panel, shows the distributions of $\Phi(\Delta\phi)$ for TT{8,9} and TT{20,50} individually, and for TT{20,50}-TT{8,9}, illustrating the effect of the subtraction.

Figure 4, right panel, shows the raw distribution of $\Sigma(\Delta\phi_{\text{thresh}})$, likewise for TT{8,9} and TT{20,50} individually, and for TT{20,50}-TT{8,9}. Since $\Sigma(\Delta\phi_{\text{thresh}})$ is an integral over $\Delta\phi$ beyond a specified threshold, care must be taken to ensure statistical independence of measurements for different values of the threshold. Each point in Fig. 4, right panel, is therefore generated from an exclusive subset of the data, with 10% of the data used for threshold values 0.1 and 0.2, 20% for 0.4, and 60% for 0.7. Subsets of unequal size are chosen to optimize the statistical errors.

Due to the limited statistical precision of the data, correction of the raw distributions in Fig. 4 via unfolding for background fluctuations and instrumental effects is not possible. In order to compare the Pb–Pb distributions with a reference distribution for pp collisions, we therefore impose the effects of instrumental response and Pb–Pb background fluctuations on the distribution calculated by PYTHIA for pp collisions at $\sqrt{s} = 2.76$ TeV. The instrumental response, modeled by GEANT, is dominated by tracking efficiency and momentum resolution. The effects of background fluctuations are modeled by embedding detector-level PYTHIA events into real Pb–Pb events. Recoil jets are reconstructed from these hybrid events, using the same procedures as real data analysis.

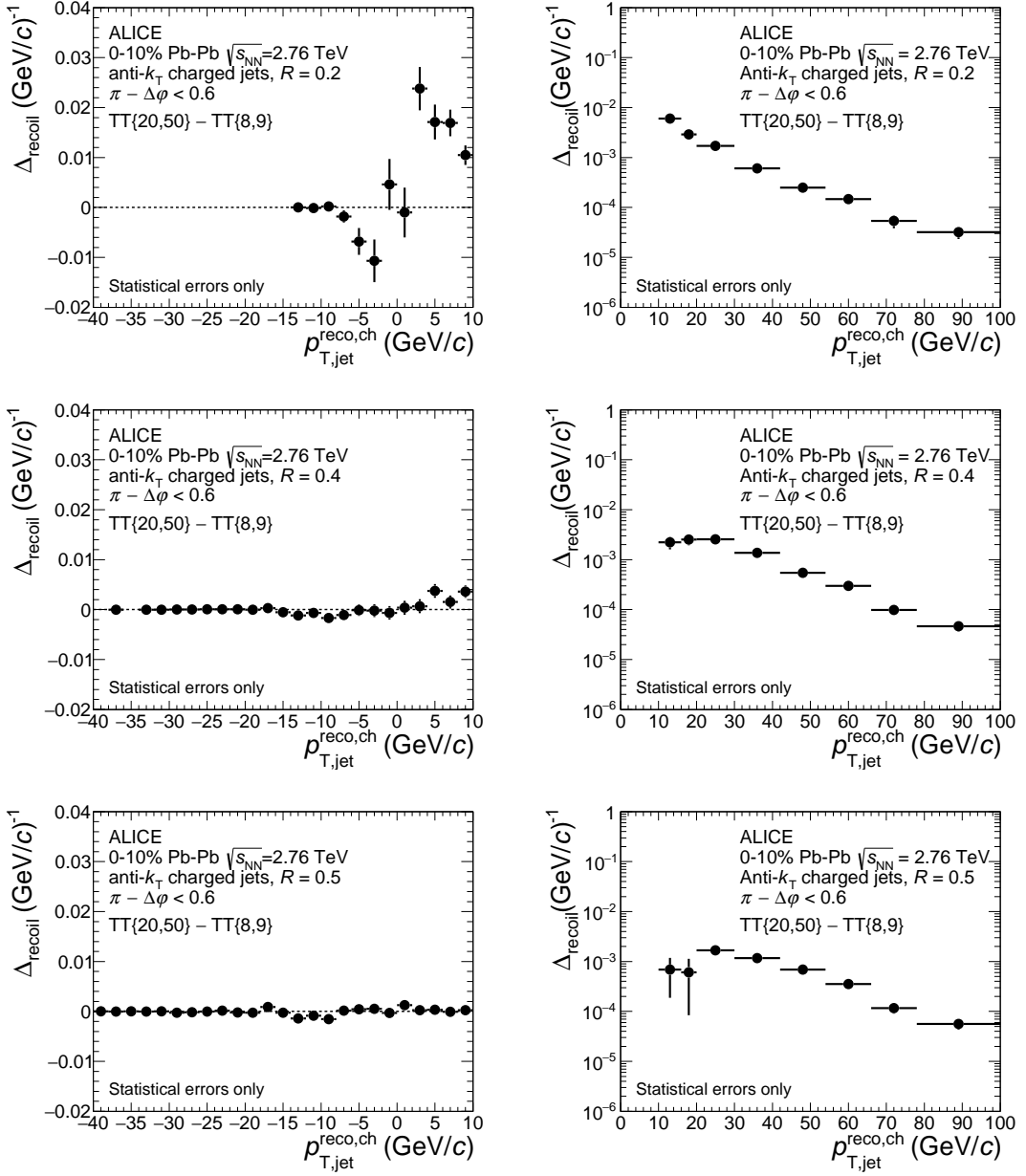


Fig. 3: Distribution of raw Δ_{recoil} for $R = 0.2, 0.4$, and 0.5 , measured in central Pb–Pb collisions for Signal TT class $\{20,50\}$ and Reference TT class $\{8,9\}$. Left panels: $p_{T,\text{jet}}^{\text{reco},\text{ch}}$ range of fit to extract c_{Ref} , with linear vertical scale. Right panels: $p_{T,\text{jet}}^{\text{reco},\text{ch}}$ range above fit region, with logarithmic vertical scale. Error bars show statistical errors only.

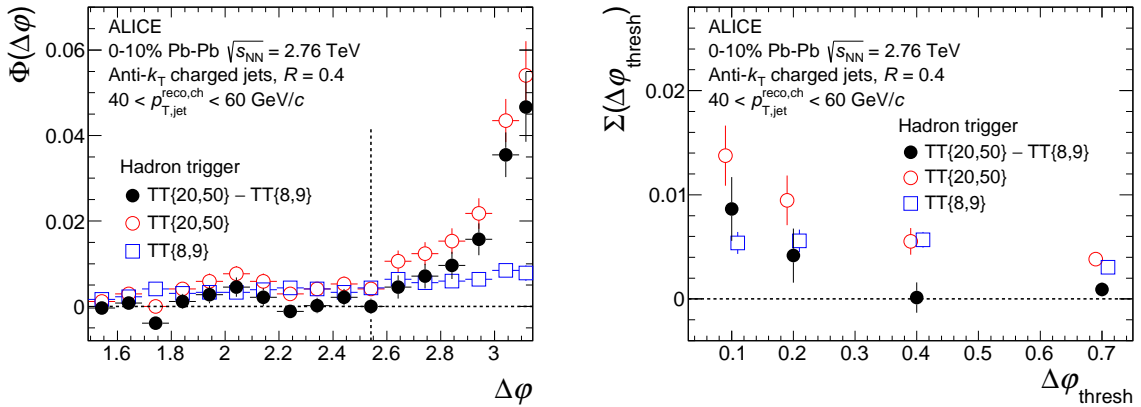


Fig. 4: $\Phi(\Delta\varphi)$ (left) and $\Sigma(\Delta\varphi_{\text{thresh}})$ (right) distributions in central Pb–Pb collisions for $\text{TT}\{20,50\}$ (open red circles), $\text{TT}\{8,9\}$ (open blue boxes), and $\text{TT}\{20,50\}-\text{TT}\{8,9\}$ (filled black circles), for jets with $40 < p_{T,\text{jet}}^{\text{reco},\text{ch}} < 60$ GeV/ c . All error bars are statistical only. The vertical dashed line in the left panel indicates the acceptance limit for the Δ_{recoil} measurement. Points in the right panel are displaced horizontally for clarity.

6 Corrections to Δ_{recoil} distributions

Corrections to the raw Δ_{recoil} distributions for underlying event fluctuations and instrumental response are carried out using unfolding methods [58, 59], in which the true jet distribution T is determined from the measured distribution M using a response matrix. We denote by R_{tot} the response matrix that incorporates all corrections, due to underlying event fluctuations and to instrumental response. R_{tot} maps $T(p_{\text{T,jet}}^{\text{part}})$ to $M(p_{\text{T,jet}}^{\text{det}})$,

$$M(p_{\text{T,jet}}^{\text{det}}) = R_{\text{tot}}(p_{\text{T,jet}}^{\text{det}}, p_{\text{T,jet}}^{\text{part}}) \times T(p_{\text{T,jet}}^{\text{part}}), \quad (7)$$

where $p_{\text{T,jet}}^{\text{part}}$ is the particle-level charged-jet p_{T} and $p_{\text{T,jet}}^{\text{det}}$ is the detector-level or reconstructed jet p_{T} .

Precise inversion of Eq. 7 for non-singular R_{tot} may result in a solution with large fluctuations in central values and large variance, arising from statistical noise in $M(p_{\text{T,jet}}^{\text{det}})$ [58]. Inversion of Eq. 7 to obtain a physically interpretable solution is achieved via regularized unfolding, which imposes the additional constraint of smoothness on the solution.

Input to the unfolding procedure uses jets in the range $20 < p_{\text{T,jet}}^{\text{det}} < 100 \text{ GeV}/c$. The distribution in Eq. 4 provides a natural cutoff at low $p_{\text{T,jet}}^{\text{det}}$, where the difference between central values of Signal and Reference distributions is smaller than the statistical error of the difference, so that imposition of a lower bound in this range is strictly speaking not required. However, in practice it was found that imposition of a lower bound at $p_{\text{T,jet}}^{\text{det}} = 20 \text{ GeV}/c$, which is above the LO cutoff in terms of charged jet $p_{\text{T,jet}}^{\text{det}}$, is needed for stable unfolding. This bound was kept as low as possible, to retain as much correlated signal as possible. The upper bound is set by the requirement that the highest $p_{\text{T,jet}}^{\text{det}}$ bin has at least 10 counts.

Correction for loss of jet yield in the excluded regions is carried out by applying a $p_{\text{T,jet}}^{\text{part}}$ -dependent efficiency ε_{kin} , which is determined using PYTHIA simulations. ε_{kin} is close to unity for all R in the analysis, over most of the range $20 < p_{\text{T,jet}}^{\text{part}} < 100 \text{ GeV}/c$. Its value is $\varepsilon_{\text{kin}} = 50\%$ at $p_{\text{T,jet}}^{\text{part}} = 20 \text{ GeV}/c$ for all R , due primarily to detector efficiency, and $\varepsilon_{\text{kin}} = 70\%$ at $p_{\text{T,jet}}^{\text{part}} = 100 \text{ GeV}/c$ for all R , due to the effects of momentum resolution and background fluctuations. The jet finding efficiency is 95% for $p_{\text{T,jet}}^{\text{part}} = 20 \text{ GeV}/c$ and 100% for $p_{\text{T,jet}}^{\text{part}} > 40 \text{ GeV}/c$, for all R .

For the Pb–Pb analysis, the primary unfolding algorithm is an iterative procedure based on Bayes’ Theorem [60], as implemented in the RooUnfold software package [61]. Regularization is imposed by requiring only small variation between successive iterations, which occurs typically after three iterations. Closure of the unfolding procedure for Δ_{recoil} was tested in model studies with correlated spectrum and background fluctuations similar to those of this measurement [57]. An alternative unfolding algorithm, regularized Singular Value Decomposition (SVD) [59], was used to estimate the systematic uncertainties.

Both unfolding algorithms were also used for the pp analysis. In this case, the SVD algorithm was used to determine the central values, while Bayesian unfolding is used to estimate the systematics. This was found to be the optimal approach for the more limited statistics of the pp distributions.

Both unfolding methods require initial specification of a prior distribution. For the Pb–Pb analysis, the prior is the Δ_{recoil} distribution for pp collisions at $\sqrt{s} = 2.76 \text{ TeV}$, calculated using PYTHIA (Perugia 10 tune). For pp collisions at $\sqrt{s} = 7 \text{ TeV}$, the prior is calculated using PYTHIA (Perugia 10 tune [32]).

6.1 Correction for instrumental response

The procedures to correct the jet energy for instrumental effects are the same as those described in [17]. The dominant correction is due to tracking efficiency, with p_{T} resolution generating the second-largest correction.

Corrections for instrumental effects are determined from simulations of pp collisions at $\sqrt{s} = 2.76$ TeV generated by PYTHIA, together with detailed detector simulations generated using GEANT followed by event reconstruction. The lower tracking efficiency in central Pb–Pb collisions was modeled by randomly discarding additional detector-level tracks. The additional rejection factor was determined by comparing Hijing and Pythia efficiencies and corresponds to 2–3%, with weak p_T dependence [20].

Jet reconstruction is carried out for each event at both the particle and detector level. The instrumental response matrix, R_{det} , is generated by associating particle-level and detector-level jets whose centroids are close in (η, ϕ) , following the procedure described in [17].

6.2 Correction for background fluctuations

The adjustment of reconstructed jet energy by the estimated background density $\rho \cdot A_{\text{jet}}^i$ (Eq. 2) accounts approximately for event-wise variation in the background level, which arises from variation in multiplicity within the 0–10% centrality percentile bin [38]. The jet energy scale of the Δ_{recoil} distribution must still be corrected for energy smearing, due to local background energy density fluctuations relative to the median background density ρ .

Background fluctuations δp_T are measured by two techniques: the Random Cone method (RC) [38], and a method in which model jets are embedded into real events [39]. The distribution of fluctuations in background energy for the RC method has RMS = 4.35 GeV/c for $R = 0.2$, 9.9 GeV/c for $R = 0.4$, and 13 GeV/c for $R = 0.5$. The RC method is used for the central data points, with the embedding method used to assess the systematic uncertainty.

The calculation of ρ (Eq. 1) requires algorithmic choices that are not unique, notably the jet reconstruction algorithm and the population of jets used for the median calculation. However, calculation of the response matrix for unfolding of background fluctuations incorporates the same set of choices. If all jet candidates are retained, without rejection based on $p_{T,\text{jet}}^{\text{det}}$, the effect of any systematic shift in JES due to ρ will be precisely counterbalanced by a shift of the same magnitude but opposite sign in the response matrix. This two-step JES correction, with event-by-event jet energy adjustment for event pedestal $\rho \cdot A_{\text{jet}}^i$ followed by ensemble-level unfolding of background fluctuations δp_T , will consequently be independent of the specific algorithmic choices for determining ρ .

In this analysis, the definition of ρ for the first step excludes the two hardest jet candidates from the median calculation (Eq. 1), while in the second step only jet candidates with $p_{T,\text{jet}}^{\text{det}} > 20$ GeV/c are used for unfolding. However, this rejection cut in the second step induces an implicit dependence on the specific definition of ρ . In order to assess this effect, the analysis was repeated with an alternative definition of ρ , in which all jet candidates are included in the median calculation in the first step. No significant differences were observed in the corrected recoil jet spectra.

6.3 Cumulative response matrix

For the Pb–Pb analysis, the cumulative response matrix R_{tot} is the product of the response matrices for instrumental response and background fluctuations. To illustrate the magnitude of corrections to Δ_{recoil} from unfolding the raw distributions with R_{tot} , we calculate the converse effect by convoluting the Δ_{recoil} distribution for pp collisions with R_{tot} . Fig. 5 compares the particle-level Δ_{recoil} distribution calculated using PYTHIA for pp collisions at $\sqrt{s} = 2.76$ TeV for $R = 0.2$ and 0.5 with their convolution with R_{det} and δp_T separately, and R_{tot} . The figure shows the ratio of the convolution over the unsmeared distribution. For $R = 0.2$, the effects of background fluctuations are small, and the net effect of R_{tot} is due primarily to the instrumental response. For $R = 0.5$, the effects of background fluctuations and instrumental response offset each other to a large degree, with only a small net effect on the central values of the distribution. The distributions for $R = 0.4$ are similar to those for $R = 0.5$. Since the shape of the Δ_{recoil} distribution is similar in the pp and Pb–Pb analyses, the corrections in the two analyses will likewise be similar.

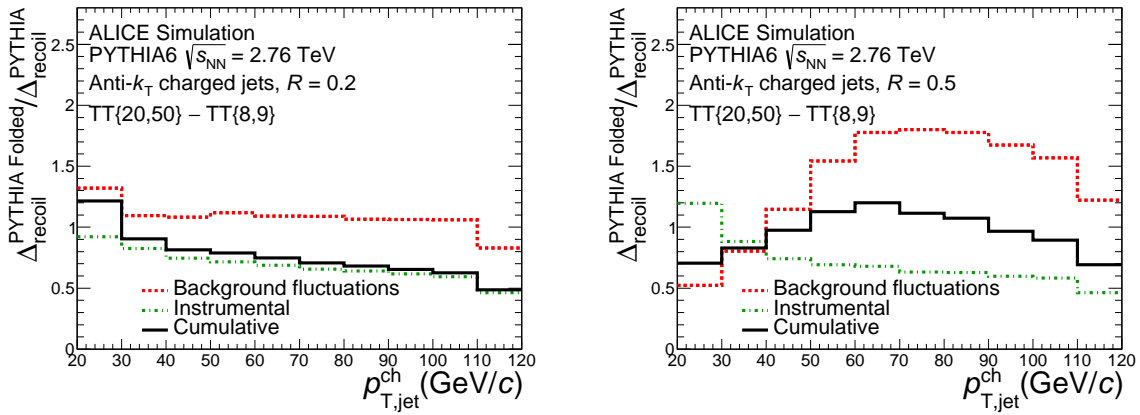


Fig. 5: Ratio of Δ_{recoil} distributions for pp collisions at $\sqrt{s} = 2.76$ TeV, for $R = 0.2$ (left) and $R = 0.5$ (right). The numerator is convoluted with R_{det} and δp_T separately, and with R_{tot} . The denominator is the unsmeared distribution.

For the pp analysis, only the instrumental response was corrected using unfolding, i.e. $R_{\text{tot}} = R_{\text{det}}$.

6.4 Other effects

In this section we discuss other effects that do not warrant correction of the data.

Since this analysis is based on a semi-inclusive observable, with normalization provided by the number of trigger hadrons measured offline, correction for online trigger efficiency (Sect. 2) is not required. No significant difference in measured distributions was observed for events in the 0-8% and 9-10% centrality intervals.

Tracking efficiency at high- p_T is 80% (Sect. 2), so that 20% of all trigger hadrons will not be observed. However, this tracking efficiency is uniform over the $p_{T,\text{trig}}$ range spanning both the Reference and Signal TT classes, so the loss in trigger statistics is unbiased in $p_{T,\text{trig}}$. Since the measurements are trigger-normalized semi-inclusive distributions, the reduction in the observed trigger hadrons corresponds simply to a loss of events, and correction for this effect is not required.

Section 4.3 presented considerations of trigger-jet energy loss in the interpretation of these measurements. A related but distinct effect is variation of R_{AA} , the suppression of inclusive hadron yield in central Pb–Pb collisions, over the $p_{T,\text{trig}}$ -interval of the Signal TT bin [13, 14]. Such a variation can generate different hard-process selection bias for the same hadron trigger cuts in pp and Pb–Pb collisions, even if trigger-jet energy loss effects in Pb–Pb are negligible. Using PYTHIA simulations, we estimate that this variation may generate an increase in Δ_{recoil} of 5% at $p_{T,\text{jet}} = 20$ GeV/c and 15% at $p_{T,\text{jet}} = 100$ GeV/c, but negligible change in the ratio of Δ_{recoil} in Pb–Pb with different R (see Fig. 10 and discussion below). Such effects will however be included in theoretical calculations which incorporate quenching and accurately reproduce the measured p_T -dependence of inclusive hadron R_{AA} , and we do not correct the data for them.

High- $p_{T,\text{trig}}$ hadron triggers above a fixed p_T threshold bias the event population due to correlation with the Event plane (EP) orientation, and bias towards more-central events. Both effects will bias the underlying event density and its fluctuations in the recoil jet region. Note, however, that for the $p_{T,\text{trig}}$ ranges of the Signal and Reference TT classes in this analysis, the second-order EP correlation amplitude v_2 exhibits no significant variation with hadron p_T ($v_2 \approx 0.01$ for $p_T > 10$ GeV/c [62, 63]), and the centrality bias is also invariant. The subtraction of the two distributions in Δ_{recoil} and $\Phi(\Delta\phi)$ thereby removes the effect of such background biases to a significant extent. Residual effects of these biases are assessed in Sect. 7, and are included in the systematic uncertainties.

Multiple, incoherent partonic interactions (MPI) can generate both a trigger hadron and uncorrelated hard jets in the recoil acceptance, in the same Pb–Pb collision. A recent analysis of γ -jet coincidences corrected for this background using a mixed event technique [43]. Since the rate of uncorrelated hard interactions is by definition independent of $p_{T,\text{trig}}$, the subtraction of the Reference from the Signal distribution in Eq. 4 and Eq. 5 suppresses entirely the contribution of jet candidates from all uncorrelated sources, including jets found in the recoil acceptance arising from MPI. Correction for MPI effects is therefore not required, for all observables considered in this analysis.

7 Systematic uncertainties

7.1 Systematic uncertainties of Δ_{recoil}

The systematic uncertainties for the distributions from Pb–Pb collisions are determined by varying parameters and algorithmic choices in corrections for instrumental response and background fluctuations. For the Δ_{recoil} distribution for pp collisions at $\sqrt{s} = 7$ TeV, systematic uncertainties are determined by varying the corrections for the instrumental response.

The significant systematic uncertainties of the Δ_{recoil} distributions in Pb–Pb collisions are as follows:

- Fit range for c_{Ref} (Table 1): variation of limits for fit generates a variation in Δ_{recoil} of less than 1%;
- Tracking efficiency: variation of R_{det} by changing the tracking efficiency by 5% generates a variation in corrected Δ_{recoil} of 4% at $p_{T,\text{jet}}^{\text{ch}} \approx 20$ GeV/c and 15% at $p_{T,\text{jet}}^{\text{ch}} \approx 100$ GeV/c;
- Fragmentation model for instrumental response: determination of R_{det} using PYQUEN rather than PYTHIA. PYQUEN has large-angle radiation enabled and was tuned to LHC data [64]. This gives a variation in Δ_{recoil} of 2% at $p_{T,\text{jet}}^{\text{ch}} \approx 20$ GeV/c and 13% at $p_{T,\text{jet}}^{\text{ch}} \approx 100$ GeV/c;
- Event plane and multiplicity bias: the trigger hadron yield and background fluctuation distributions are measured differentially in bins of azimuthal angle relative to the EP. The trigger hadron yield is found to be correlated with EP orientation, indicating non-zero elliptic flow. The response matrix is then obtained by weighting the azimuth-dependent background fluctuation distribution with the azimuth-dependent trigger hadron yield. The change in corrected jet yield with and without this weighting is less than 5%. The effects of the multiplicity bias are negligible;
- Background fluctuations: using embedding rather than the RC method to measure background fluctuations (Sect. 6.2) generates differences in the corrected Δ_{recoil} distribution of less than 10%;
- Variation in unfolding algorithm: termination of Bayesian unfolding after five rather than three iterations generates variations in Δ_{recoil} of $\approx 1\%$ over most of the measured range. SVD unfolding yields Δ_{recoil} distributions that differ from the Bayesian-based corrected distributions by 1%;
- Choice of unfolding prior: for Bayesian-based unfolding, the alternative priors are the Δ_{recoil} distribution for pp collisions at $\sqrt{s} = 2.76$ TeV including a 10% or 20% relative energy shift, to model jet energy loss. For SVD unfolding, the alternative prior is the Bayesian-based unfolded distribution. The largest variation in the corrected Δ_{recoil} is less than 6% at all $p_{T,\text{jet}}^{\text{ch}}$;
- Spectrum binning and limits: variations of upper and lower spectrum limits generate variations in corrected Δ_{recoil} of less than 3% at low $p_{T,\text{jet}}^{\text{ch}}$, with negligible variation at high $p_{T,\text{jet}}^{\text{ch}}$. Variation in choice of binning generates changes in corrected Δ_{recoil} that are less than 4%.

The products of weak decays make negligible contribution to $p_{T,\text{jet}}^{\text{ch}}$ because of the stringent track selection requirements of the analysis and the low material budget of the ITS and TPC. The systematic uncertainty of Δ_{recoil} due to the contribution of secondary vertex decays is less than 2%.

Systematic uncertainty	$p_{T,\text{jet}}^{\text{ch}} = 25 \text{ GeV}/c$	$p_{T,\text{jet}}^{\text{ch}} = 75 \text{ GeV}/c$
Correlated		
Scale Factor c_{Ref}	(-1,+0)%	(-0,+0.1)%
Tracking efficiency	(-6,+6)%	(-16,+16)%
Fragmentation model	(-0,+2)%	(-0,+14)%
EP bias	(-2,+0)%	(-3,+0)%
Uncorrelated or shape		
Background fluctuations	(-0,+7)%	(-0,+8)%
Unfolding algorithm	(-0,+1)%	(-0,+2)%
Unfolding prior	(-5,+0)%	(-11,+6)%
Spectrum limits and binning	(-1,+0)%	(-2,+3)%
Cumulative correlated uncertainty	(-7,+6)%	(-17,+22)%
Cumulative uncorrelated uncertainty	(-5,+7)%	(-11,+11)%

Table 2: Relative systematic uncertainties of Δ_{recoil} , for $R = 0.4$ jets and two values of $p_{T,\text{jet}}^{\text{ch}}$ for central Pb–Pb collisions at $\sqrt{s_{\text{NN}}} = 2.76 \text{ TeV}$, TT{20,50}-TT{8,9}. Uncertainties are expressed as negative and positive differences from the central values, with an entry of zero indicating negligible contribution. Uncertainties are classified as correlated and uncorrelated, as described in the text.

Table 2 presents the significant systematic uncertainties for $R = 0.4$, at two values of $p_{T,\text{jet}}^{\text{ch}}$. Uncertainties are presented as the relative difference to the central values of the corrected Δ_{recoil} . We distinguish between correlated systematic uncertainties, arising from variations that generate a correlated change in the magnitude of the spectrum, and uncorrelated (or shape) uncertainties, arising from variations that preserve the integral but generate a change in the shape of the spectrum. Cumulative uncertainties are the quadratic sum of all correlated or uncorrelated uncertainties. Uncertainties for $R = 0.2$ and 0.5 are evaluated in a similar way.

Similar systematic uncertainties were considered for the Δ_{recoil} distribution in pp collisions at $\sqrt{s} = 7 \text{ TeV}$ as those discussed for Pb–Pb collisions. Uncertainty in tracking efficiency causes variation in Δ_{recoil} by 2% at $p_{T,\text{jet}} \approx 20 \text{ GeV}/c$ and 9% at $p_{T,\text{jet}} \approx 60 \text{ GeV}/c$. The systematic uncertainty due to track momentum resolution is estimated to be 4% in the entire p_T range. The shift of jet energy scale due to contamination by secondary particles and fake tracks causes a variation in Δ_{recoil} of less than 2%. Variations in the unfolding procedure, including change in the choice of unfolding algorithm, prior, and spectrum binning, result in Δ_{recoil} changes of $\approx 5\%$. The cumulative systematic uncertainty is given by the quadratic sum of all individual uncertainties.

7.2 Systematic uncertainties of $\Phi(\Delta\phi)$ and $\Sigma(\Delta\phi_{\text{thresh}})$

The systematic uncertainties for the measurement of $\Phi(\Delta\phi)$ and $\Sigma(\Delta\phi_{\text{thresh}})$ are presented in this section.

- Since the yield of correlated hard jets decreases with increasing acoplanarity (i.e. increasing $|\Delta\phi - \pi|$), the scale factor c_{Ref} in this region should approach unity. To assess this effect, c_{Ref} is varied from its nominal values in Table 1 to unity. The resulting change in width of the uncorrected $\Phi(\Delta\phi)$ distribution (Eq.8) is 0.001 and the change in slope of the $\Sigma(\Delta\phi_{\text{thresh}})$ ratio (Fig. 12) is 0.35, which are taken as the systematic uncertainties.

- Tracking efficiency less than unity will result in jets that are reconstructed from a subset of their charged track constituents, with consequent variation of jet centroid. However, the 5% relative uncertainty of tracking efficiency generates negligible variation in the width of the $\Phi(\Delta\phi)$ distribution and in the slope of the $\Sigma(\Delta\phi_{\text{thresh}})$ ratio.
- The EP bias due to the hadron trigger, discussed in Sect. 7.1, generates a change of 0.005 in the width of the $\Phi(\Delta\phi)$ and 0.07 in the slope of the $\Sigma(\Delta\phi_{\text{thresh}})$ ratio.

Systematic uncertainty	Width of $\Phi(\Delta\phi)$	Slope of $\Sigma(\Delta\phi_{\text{thresh}})$ ratio
Scale factor c_{Ref}	± 0.001	± 0.35
Tracking efficiency	negligible	negligible
EP bias	± 0.005	± 0.07
Cumulative uncertainty	± 0.005	± 0.36

Table 3: Systematic uncertainties for the width of the $\Phi(\Delta\phi)$ distribution (Eq.8) and the slope of the $\Sigma(\Delta\phi_{\text{thresh}})$ ratio (Fig. 12, right panel). The cumulative uncertainty is the quadratic sum of all contributions.

Table 3 shows all sources of systematic uncertainty for $\Phi(\Delta\phi)$ and $\Sigma(\Delta\phi_{\text{thresh}})$, with the cumulative uncertainty given by their quadratic sum. Instrumental effects generate negligible uncertainty in the azimuthal correlations.

8 Distributions for pp collisions at $\sqrt{s} = 2.76$ TeV

As noted above, comparison of Pb–Pb measurements to similar distributions in pp collisions at $\sqrt{s} = 2.76$ TeV requires calculations based on PYTHIA and NLO pQCD. In order to validate this approach, we compare PYTHIA and NLO pQCD-based calculations to ALICE measurements of Δ_{recoil} distributions in pp collisions at $\sqrt{s} = 7$ TeV, using the data shown in Fig. 1.

The NLO pQCD-based framework was developed initially to calculate the spin-dependent hadron-jet coincidence cross section at $\sqrt{s} = 200$ GeV [27]. The calculation uses the DSS fragmentation function [65] and the CT10 NLO parton distribution function [66]. We model hadronization by a shift in p_{T} for parton-level jets [67], with the magnitude of the shift determined by a fit to inclusive jet distributions [68]. The resulting particle-level jet distribution is transformed to a charged-jet distribution by applying a response matrix calculated using PYTHIA. The systematic uncertainty of the resulting spectrum is estimated by independently varying the parton distribution function and the factorization and renormalization scales by a factor two.

Figure 6, upper panels, show Δ_{recoil} distributions for $R = 0.5$, from ALICE data and calculations for pp collisions at $\sqrt{s} = 7$ TeV. The lower panels show the ratios of these distributions to a function which parameterizes the ALICE data. The PYTHIA calculations for both tunes agree with the measurement within uncertainties; similar agreement is found for $R = 0.2$ and 0.4 . The central values of the NLO calculation are above the measured data by about 20%, though the calculation is consistent with data within uncertainties for $R = 0.5$. The discrepancy in central values is larger for smaller R , reaching about 50% for $R = 0.2$, which is not consistent within systematic uncertainties. In pQCD calculations the difference between the parton and jet momenta involves an expansion in terms of $\log(R)$, whose contribution may be significant for small R [69]. Improved agreement between the NLO calculation and data for $R = 0.2$ may therefore be achievable using resummation techniques [69].

Figure 7 shows the ratio of Δ_{recoil} distributions for $R = 0.2$ and 0.5 in pp collisions at $\sqrt{s} = 7$ TeV. The measured ratio is compared with PYTHIA and NLO pQCD-based calculations. The grey boxes show the systematic uncertainty of the measured ratio, taking into account correlations of numerator and denominator.

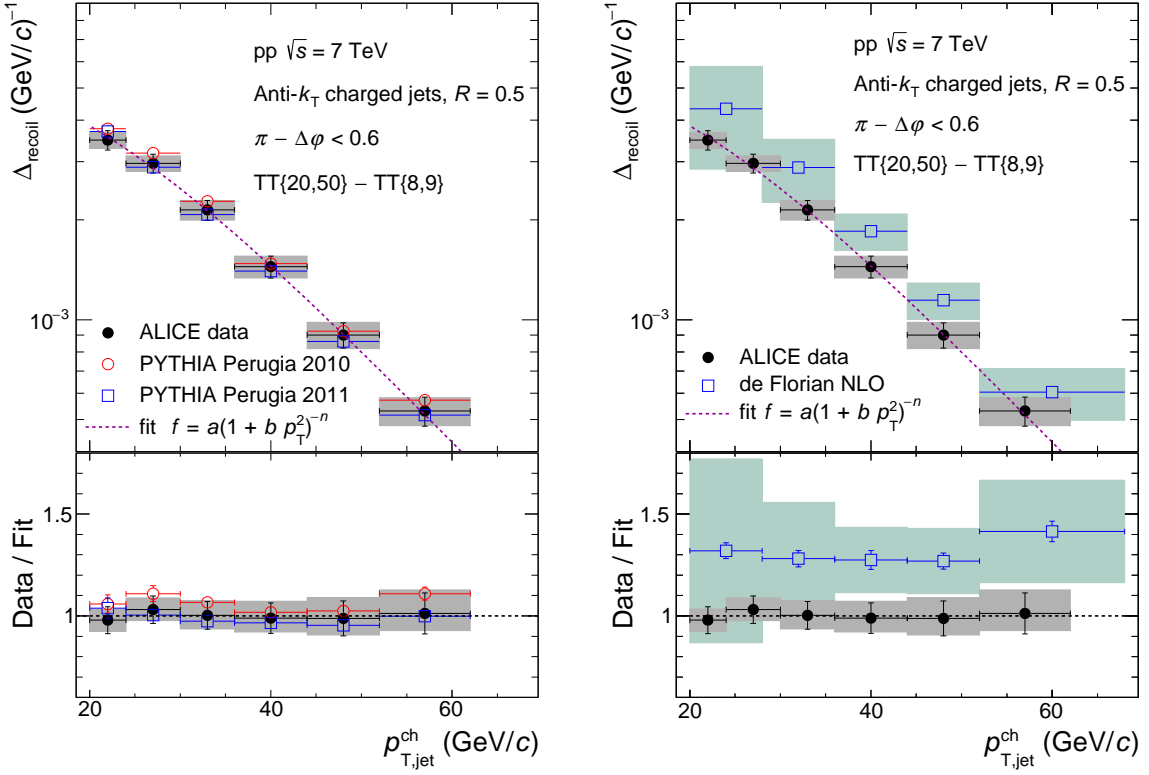


Fig. 6: Δ_{recoil} distributions for $R = 0.5$, for ALICE data and calculations of pp collisions $\sqrt{s} = 7$ TeV. ALICE data, which are the same in both panels, are compared with calculations based on PYTHIA (left) and NLO pQCD (right). The green boxes in the right panel show the systematic uncertainty of the NLO calculation. The lower panels show the ratios of data and calculations to a smooth function fit to the data.

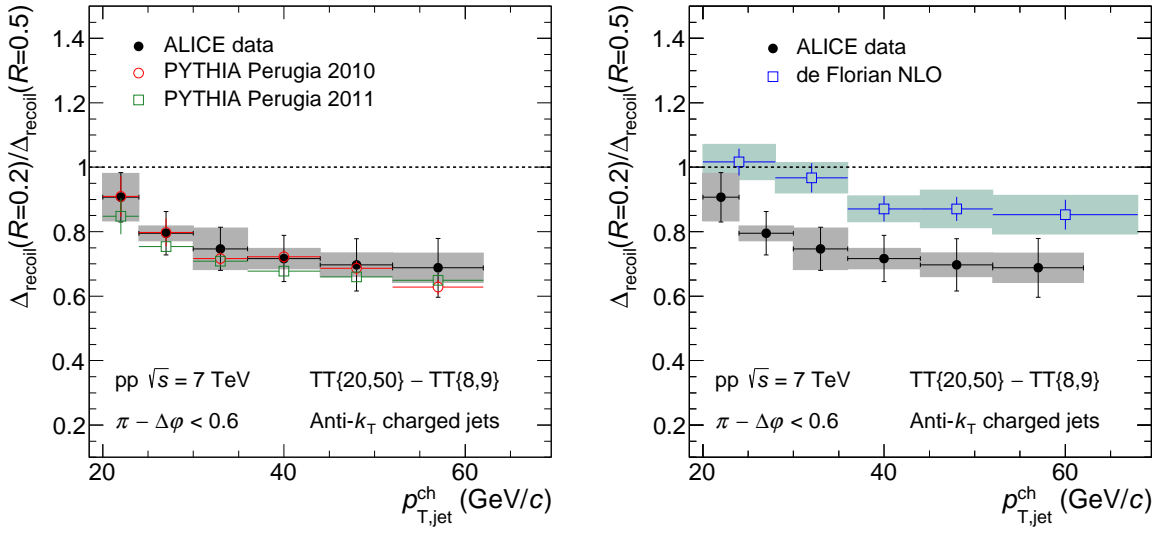


Fig. 7: Ratio of Δ_{recoil} distributions with $R = 0.2$ and 0.5 , for ALICE data and calculations from pp collisions at $\sqrt{s} = 7$ TeV. ALICE data, which are the same in both panels, are compared with calculations using PYTHIA (left) and NLO pQCD (right).

The NLO calculation generates larger ratios than those observed in the data. A related observable, the ratio of inclusive jet production cross sections for $R = 0.2$ and 0.4 in pp collisions at $\sqrt{s} = 2.76$ TeV,

has also been compared with pQCD calculations [70]. This comparison shows that both hadronization corrections and perturbative effects that are effectively next-to-next-to-leading order (NNLO) in the individual cross sections [68] are required for agreement. Perturbative QCD calculations to higher order than NLO are also needed to describe the ratio of Δ_{recoil} distributions presented here.

In contrast, PYTHIA simulations agree within uncertainties with data, both for Δ_{recoil} at fixed R and the Δ_{recoil} ratio for two different values of R . These comparisons therefore favor PYTHIA calculations for the reference distributions at $\sqrt{s} = 2.76$ TeV. PYTHIA combines a LO matrix element with a parton shower resummation of leading logarithmic terms of soft gluon radiation at all orders, leading to an improved description of data compared to a fixed order analytic calculation.

9 Results

9.1 Δ_{recoil}

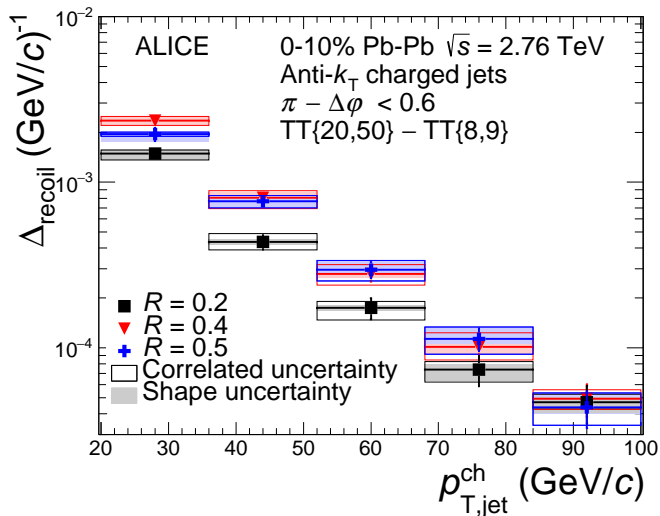


Fig. 8: Δ_{recoil} for 0-10% central Pb–Pb collisions at $\sqrt{s_{\text{NN}}} = 2.76$ TeV for anti- k_{T} jets with $R = 0.2, 0.4$ and 0.5 . The vertical error bars are the square root of the diagonal elements of the unfolding covariance matrix, with the boxes indicating correlated and uncorrelated (shape) systematic uncertainties.

Figure 8 shows corrected Δ_{recoil} distributions for central Pb–Pb collisions, for $R = 0.2, 0.4$ and 0.5 . The shape of the distributions is approximately exponential, with larger per-trigger yield for $R = 0.4$ and 0.5 than for $R = 0.2$.

The R dependence of Δ_{recoil} is related to the distribution of jet energy transverse to the jet axis. Scattering of the parton shower within the hot QCD medium may broaden this distribution [28, 71]. The magnitude of intra-jet broadening can be measured by comparing Δ_{recoil} distributions for Pb–Pb collisions with those for pp collisions, in which jets are generated in vacuum. We utilize two related observables for this purpose: (i) ΔI_{AA} , which is the ratio of Δ_{recoil} for Pb–Pb to that for pp collisions simulated using PYTHIA, for fixed R , and (ii) the ratio of Δ_{recoil} at two different R in Pb–Pb, compared with that in pp collisions.

Figure 9 shows ΔI_{AA} for $R = 0.2, 0.4$ and 0.5 . Suppression of the yield of recoil jets in Pb–Pb collisions is observed, with similar magnitude for all R .

Figure 10 shows the ratio of Δ_{recoil} for $R = 0.2$ relative to Δ_{recoil} for $R = 0.4$ and 0.5 , in central Pb–Pb and pp collisions. The systematic uncertainties of the Pb–Pb ratios take into account the correlated systematic uncertainties in numerator and denominator. The shape uncertainties are propagated independently in the

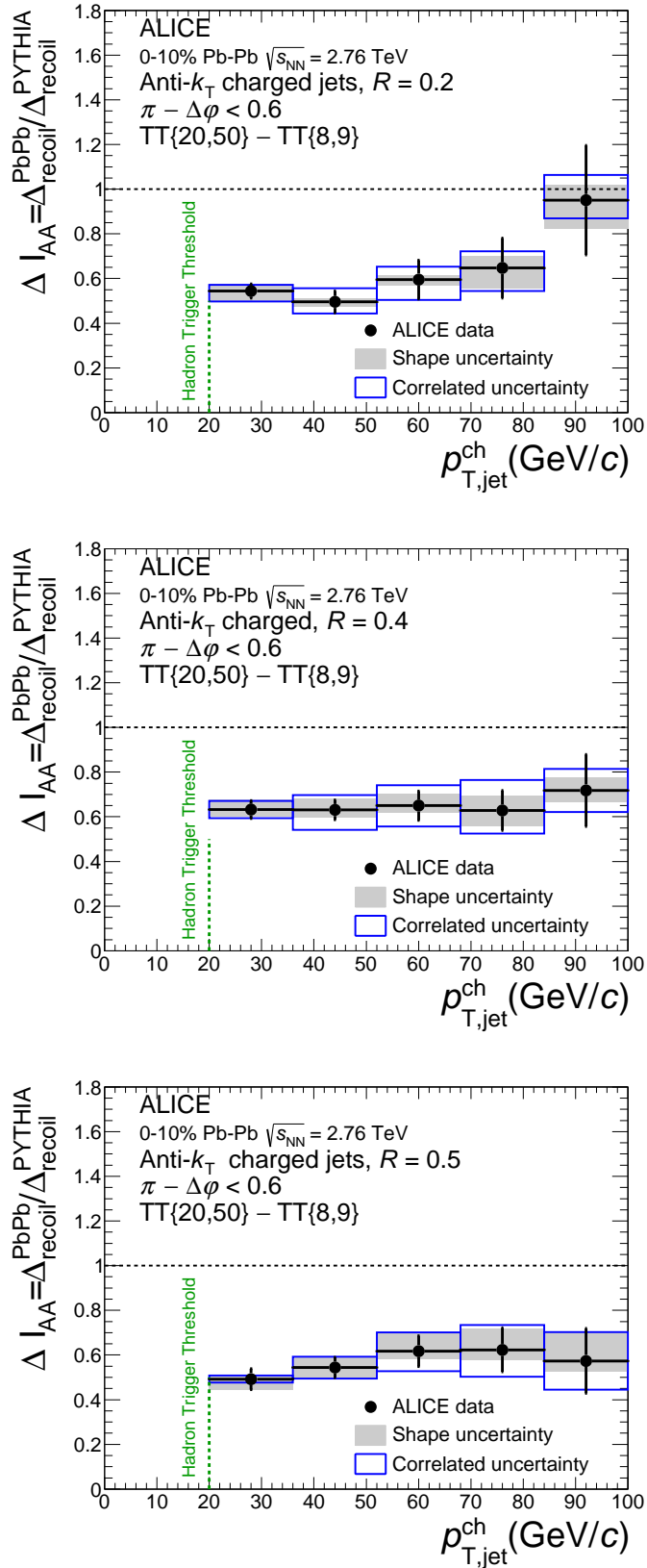


Fig. 9: ΔI_{AA} , the ratio of Δ_{recoil} in central Pb–Pb and pp collisions at $\sqrt{s} = 2.76$ TeV, for $R = 0.2, 0.4$ and 0.5 . Δ_{recoil} for pp collisions are calculated using PYTHIA.

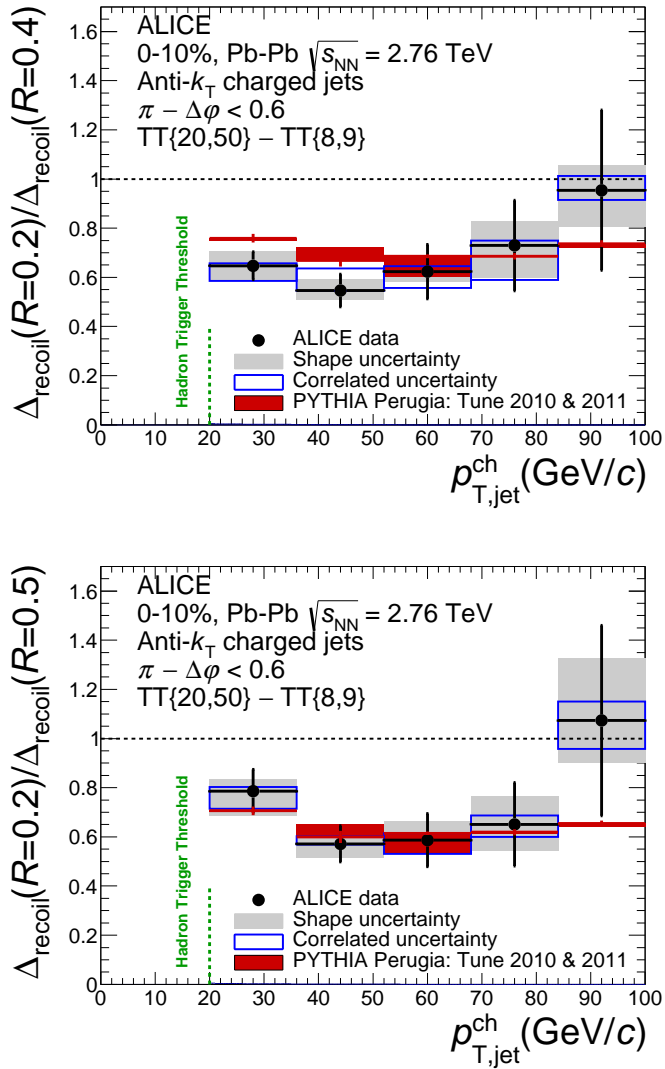


Fig. 10: Ratio of Δ_{recoil} for $R = 0.2$ relative to $R = 0.4$ (top) and to $R = 0.5$ (bottom), for central Pb–Pb (black) and pp collisions simulated using PYTHIA (red) at $\sqrt{s} = 2.76 \text{ TeV}$.

ratio, since variation in their components induces different effects as a function of R . The distributions for Pb–Pb and pp collisions are seen to be similar, with no evidence for intra-jet broadening in central Pb–Pb collisions within the uncertainties.

The CMS collaboration has reported a significant redistribution of energy within $R < 0.3$ for jets in central Pb–Pb collisions [72], potentially in contrast to Fig. 10. However, that measurement and the one reported here cannot be compared directly. Modeling of the two measurements within the same theoretical framework is required for their comparison.

Figures 9 and 10 show that the recoil jet yield is suppressed, while the intra-jet energy profile is not changed significantly for $R \leq 0.5$. We note in addition that the infrared cutoff for jet constituents (tracks) in this measurement is $p_{T,\text{const}} = 0.15 \text{ GeV}/c$, which strongly constrains the correlated energy within the jet cone that would not be detected by this measurement.

Taken together, these observations are consistent with a picture in which there is significant in-medium transport of radiation to angles larger than 0.5 radians. This picture was initially suggested by a measurement showing that the energy imbalance of highly asymmetric jet pairs is compensated, on an ensemble-

averaged basis, by the energy carried by soft particles at large angles relative to the jet axis [23]. Also in this case, however, quantitative comparison of these measurements requires their calculation in a common theoretical framework.

The Δ_{recoil} distributions in both pp and Pb–Pb collisions are well-described by an exponential distribution $\propto e^{-p_{T,\text{jet}}^{\text{ch}}/b}$, with values of b around 16 GeV/ c . Fig. 9 shows that ΔI_{AA} has negligible dependence on $p_{T,\text{jet}}^{\text{ch}}$ for $R = 0.4$ and 0.5 within $60 < p_{T,\text{jet}}^{\text{ch}} < 100$ GeV/ c , which indicates that the values of b are similar within this $p_{T,\text{jet}}$ range for the pp and Pb–Pb distributions. The value of ΔI_{AA} in this region can therefore be expressed as the horizontal shift of an exponential distribution of fixed slope. For $R = 0.5$ in the range $60 < p_{T,\text{jet}}^{\text{ch}} < 100$ GeV/ c , the suppression in ΔI_{AA} corresponds to a shift in $p_{T,\text{jet}}^{\text{ch}}$ of -8 ± 2 (stat) GeV/ c . In the scenario of negligible trigger-jet energy loss, this shift corresponds to the average partonic energy loss of the recoil jet population via energy transport to large angles, outside the jet cone.

9.2 Azimuthal correlations

Figure 11 shows the uncorrected $\Phi(\Delta\varphi)$ distributions for central Pb–Pb data and pp simulations. As noted in Sect. 5.2, we compare the uncorrected $\Phi(\Delta\varphi)$ distribution of Pb–Pb data to a reference distribution for pp collisions (PYTHIA, Perugia 2010 tune), modified by the background and instrumental effects expected for central Pb–Pb collisions. We recall that $\Phi(\Delta\varphi)$ suppresses the uncorrelated contribution from MPI, which otherwise would provide a significant background at large $\pi - \Delta\varphi$.

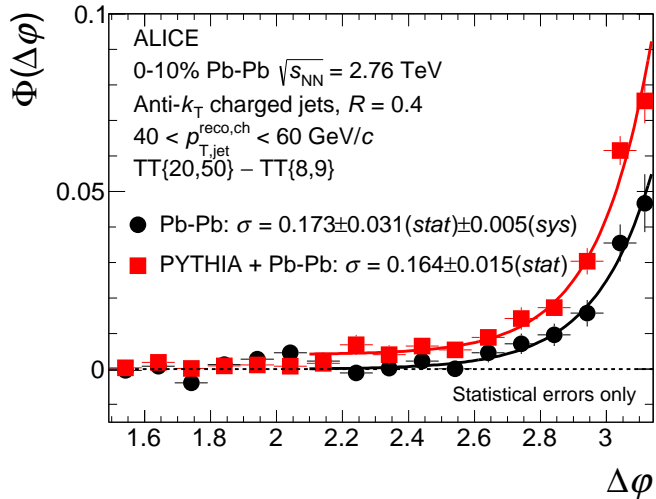


Fig. 11: $\Phi(\Delta\varphi)$ distributions for 0–10% central Pb–Pb data (black circles) and pp collisions simulated by detector-level PYTHIA events embedded into central Pb–Pb events (red squares), at $\sqrt{s_{\text{NN}}} = 2.76$ TeV. Jets have $40 < p_{T,\text{jet}}^{\text{reco},\text{ch}} < 60$, with $p_{T,\text{jet}}^{\text{reco},\text{ch}}$ not corrected for background fluctuations and instrumental effects. The lines show the result of fitting Eq. 8 to the distributions, with the value of σ from the fit as indicated. The error bars show statistical errors only. The Pb–Pb data points are the same as the solid circles shown in the left panel of Fig. 4.

The absolute yield of the Pb–Pb distribution is seen to be smaller than that of the pp reference. This is consistent with the suppression observed for ΔI_{AA} (Fig. 9), which is the ratio of the integrals of the $\Phi(\Delta\varphi)$ distributions over the range $\pi - \Delta\varphi < 0.6$.

The $\Phi(\Delta\varphi)$ distributions for Pb–Pb and pp collisions are characterized by fitting a function corresponding to an exponential plus a pedestal term [43],

$$f(\Delta\varphi) = p_0 \times e^{(\Delta\varphi - \pi)/\sigma} + p_1, \quad (8)$$

where the parameter σ reflects the width of the distribution. The fit range is $2\pi/3 < \Delta\varphi < \pi$. The fitted values are $\sigma_{\text{Pb–Pb}} = 0.173 \pm 0.031(\text{stat.}) \pm 0.005(\text{sys.})$ and $\sigma_{\text{PYTHIA}} = 0.164 \pm 0.015(\text{stat.})$, which are consistent within uncertainties. We find no evidence from this comparison for medium-induced acoplanarity of recoil jets with uncorrected energy in the range $40 < p_{\text{T,jet}}^{\text{reco,ch}} < 60 \text{ GeV}/c$.

The azimuthal distribution between a direct photon ($p_{T,\gamma} > 60 \text{ GeV}/c$) and a recoil jet ($p_{T,\text{jet}} > 30 \text{ GeV}/c$) has been measured in central Pb–Pb collisions and compared to that from PYTHIA events embedded in a simulation of Pb–Pb collisions [43]. Fits of an exponential function to these distributions give similar values of σ for central Pb–Pb and embedded PYTHIA, likewise indicating no evidence for medium-induced acoplanarity, though the values of σ are larger than those for the analysis reported here. Comparison of the shape of the azimuthal distribution of di-jet pairs in central Pb–Pb data and embedded PYTHIA events has been reported [22, 23], with indication of an enhancement in the tail of the distribution for central Pb–Pb collisions [22].

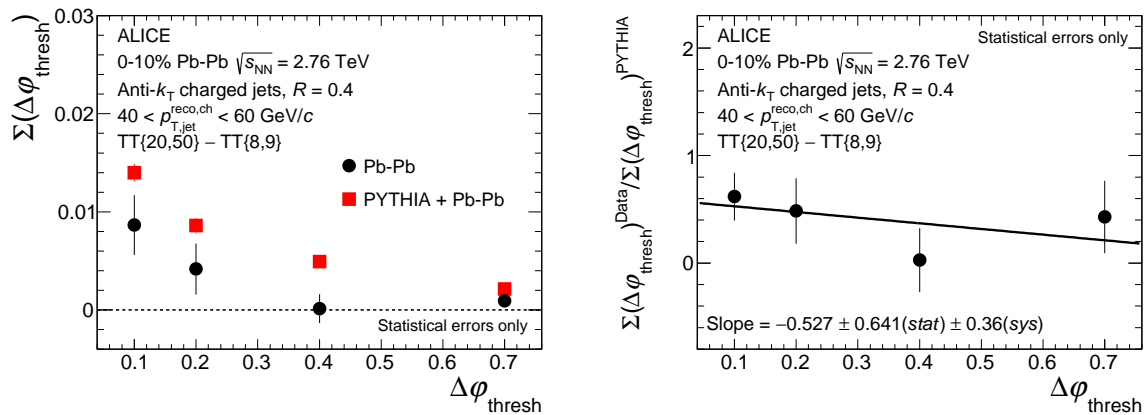


Fig. 12: Left: $\Sigma(\Delta\varphi_{\text{thresh}})$ distributions for central Pb–Pb data (black circles) and the pp reference distribution (red squares), obtained by embedding detector-level PYTHIA events into real data. Right: ratio of the $\Sigma(\Delta\varphi_{\text{thresh}})$ distribution between Pb–Pb data and the PYTHIA reference shown in the left along with a first-order polynomial fit. The error bars in both panels show statistical errors only.

More detailed characterization of the change in the angular distribution with change in TT interval is provided by $\Sigma(\Delta\varphi_{\text{thresh}})$ (Eq. 6), which measures the yield in the tail of the distribution beyond a threshold, $\pi/2 < \Delta\varphi < \pi - \Delta\varphi_{\text{thresh}}$. Fig. 12, left panel, shows the $\Sigma(\Delta\varphi_{\text{thresh}})$ distributions for central Pb–Pb data and the embedded PYTHIA reference. As discussed in Sect. 5.2, for the measurement of $\Sigma(\Delta\varphi_{\text{thresh}})$ the dataset is divided into exclusive subsets, with each subset used for only one value of threshold, so that the data points in Fig. 12 are statistically uncorrelated.

The relative contribution to $\Sigma(\Delta\varphi_{\text{thresh}})$ of different physics processes may vary with $\Delta\varphi_{\text{thresh}}$. At sufficiently large angular deflection of the jet centroid, at a value of $\Delta\varphi_{\text{thresh}}$ which has not yet been determined, the yield is expected to arise predominantly from single hard (Molière) scattering in the hot QCD medium [3, 28]. Figure 12, right panel, shows the ratio of the two distributions in the left panel. We utilize this ratio of absolutely normalized distributions in pp and Pb–Pb collisions to search for effects due to Molière scattering.

The value of the ratio at small $\Delta\varphi_{\text{thresh}}$ corresponds approximately to the $\Delta\varphi$ -integrated suppression in recoil yield in Fig. 9, while its dependence on $\Delta\varphi_{\text{thresh}}$ provides a comparison of the shapes of the distributions. This comparison is quantified by fitting a first-order polynomial function to the ratio of $\Sigma(\Delta\varphi_{\text{thresh}})$ in the right panel. The fit gives a slope of $-0.527 \pm 0.641(\text{stat.}) \pm 0.36(\text{sys.})$, which is consistent with zero within uncertainties. If Molière scattering were the only mechanism modifying the Pb–Pb distribution relative to that of pp collisions the ratio at large $\Delta\varphi_{\text{thresh}}$ should be larger than unity; however, the

ratio is seen to be below unity at the largest measured $\Delta\phi_{\text{thresh}}$, indicating that other mechanisms have large effect in this region. We find no evidence from this measurement for medium-induced Molière scattering. The uncertainty in this measurement is dominated by the statistical error, however, meaning that additional data, together with measurements at other jet energies and larger angular deviations, will provide more precise constraints on the rate of large-angle scattering in the hot QCD medium.

10 Summary

We have reported measurements of jet quenching in central Pb–Pb collisions at the LHC, using a new analysis method based on the semi-inclusive distribution of jets recoiling from a high- p_{T} trigger hadron. Discrimination of coincident jet yield from background is carried out at the level of ensemble-averaged distributions with a trigger-difference technique, with no selection bias imposed on the recoil jet population. This approach enables measurement of the distribution of jets with large R and low infrared cutoff for jet constituents, over a broad range of jet energy. Distributions are reported for charged jets in the range $20 < p_{\text{T},\text{jet}}^{\text{ch}} < 100 \text{ GeV}/c$, for $R = 0.2, 0.4$ and 0.5 .

The differential recoil jet yield in central Pb–Pb collisions is suppressed relative to that in pp collisions by up to a factor two for $0.2 \leq R \leq 0.5$. Together with the low infrared cutoff of this measurement, this indicates that medium-induced energy loss arises predominantly from radiation at angles larger than 0.5 relative to the jet axis. The energy carried by this radiation, which is reflected in the magnitude of the spectrum shift under the assumption of negligible trigger-jet energy loss, is estimated to be $8 \pm 2 \text{ GeV}/c$ for charged jets with $R = 0.5$, in the range $60 < p_{\text{T},\text{jet}}^{\text{ch}} < 100 \text{ GeV}/c$.

The ratio of differential recoil jet yields with different R is similar for Pb–Pb and pp collisions. No significant medium-induced modification of the intra-jet energy distribution for angles $R \leq 0.5$ relative to the jet axis is thereby observed.

The width of the azimuthal distribution of recoil jets relative to the trigger axis is measured to be similar in Pb–Pb and pp collisions for jets of $40 < p_{\text{T},\text{jet}}^{\text{reco},\text{ch}} < 60 \text{ GeV}/c$. No significant medium-induced acoplanarity is therefore observed, consistent with findings from di-jet and direct photon-jet measurements. Large angular deflection of the recoil jet may be sensitive to the rate of single Molière scattering in the hot QCD medium and provide a direct probe of its quasi-particle degrees of freedom. We observe no significant rate of such large-angle scatterings, though with limited statistical precision at present. These data, when combined with theoretical calculations, will provide guidance for the necessary precision to achieve discriminating measurements in the future.

Acknowledgements

We thank Daniel de Florian, Francesco d’Eramo and Krishna Rajagopal for valuable discussions and calculations. The ALICE Collaboration would like to thank all its engineers and technicians for their invaluable contributions to the construction of the experiment and the CERN accelerator teams for the outstanding performance of the LHC complex. The ALICE Collaboration gratefully acknowledges the resources and support provided by all Grid centres and the Worldwide LHC Computing Grid (WLCG) collaboration. The ALICE Collaboration acknowledges the following funding agencies for their support in building and running the ALICE detector: State Committee of Science, World Federation of Scientists (WFS) and Swiss Fonds Kidagan, Armenia, Conselho Nacional de Desenvolvimento Científico e Tecnológico (CNPq), Financiadora de Estudos e Projetos (FINEP), Fundação de Amparo à Pesquisa do Estado de São Paulo (FAPESP); National Natural Science Foundation of China (NSFC), the Chinese Ministry of Education (CMOE) and the Ministry of Science and Technology of China (MSTC); Ministry of Education and Youth of the Czech Republic; Danish Natural Science Research Council, the Carlsberg Foundation and the Danish National Research Foundation; The European Research Council under the

European Community’s Seventh Framework Programme; Helsinki Institute of Physics and the Academy of Finland; French CNRS-IN2P3, the ‘Region Pays de Loire’, ‘Region Alsace’, ‘Region Auvergne’ and CEA, France; German Bundesministerium fur Bildung, Wissenschaft, Forschung und Technologie (BMBF) and the Helmholtz Association; General Secretariat for Research and Technology, Ministry of Development, Greece; Hungarian Orszagos Tudomanyos Kutatasi Alapprogrammok (OTKA) and National Office for Research and Technology (NKTH); Department of Atomic Energy and Department of Science and Technology of the Government of India; Istituto Nazionale di Fisica Nucleare (INFN) and Centro Fermi - Museo Storico della Fisica e Centro Studi e Ricerche ”Enrico Fermi”, Italy; MEXT Grant-in-Aid for Specially Promoted Research, Japan; Joint Institute for Nuclear Research, Dubna; National Research Foundation of Korea (NRF); Consejo Nacional de Ciencia y Tecnología (CONACYT), Dirección General de Asuntos del Personal Académico (DGAPA), México, Amerique Latine Formation académique - European Commission (ALFA-EC) and the EPLANET Program (European Particle Physics Latin American Network); Stichting voor Fundamenteel Onderzoek der Materie (FOM) and the Nederlandse Organisatie voor Wetenschappelijk Onderzoek (NWO), Netherlands; Research Council of Norway (NFR); National Science Centre, Poland; Ministry of National Education/Institute for Atomic Physics and Consiliul Naional al Cercetrii inovative - Executive Agency for Higher Education Research Development and Innovation Funding (CNCS-UEFISCDI) - Romania; Ministry of Education and Science of Russian Federation, Russian Academy of Sciences, Russian Federal Agency of Atomic Energy, Russian Federal Agency for Science and Innovations and The Russian Foundation for Basic Research; Ministry of Education of Slovakia; Department of Science and Technology, South Africa; Centro de Investigaciones Energeticas, Medioambientales y Tecnologicas (CIEMAT), E-Infrastructure shared between Europe and Latin America (EELA), Ministerio de Economía y Competitividad (MINECO) of Spain, Xunta de Galicia (Consejería de Educación), Centro de Aplicaciones Tecnológicas y Desarrollo Nuclear (CEADEN), Cubaenergía, Cuba, and IAEA (International Atomic Energy Agency); Swedish Research Council (VR) and Knut & Alice Wallenberg Foundation (KAW); Ukraine Ministry of Education and Science; United Kingdom Science and Technology Facilities Council (STFC); The United States Department of Energy, the United States National Science Foundation, the State of Texas, and the State of Ohio; Ministry of Science, Education and Sports of Croatia and Unity through Knowledge Fund, Croatia. Council of Scientific and Industrial Research (CSIR), New Delhi, India

References

- [1] A. Majumder and M. Van Leeuwen, “The Theory and Phenomenology of Perturbative QCD Based Jet Quenching,” *Prog.Part.Nucl.Phys.* **A66** (2011) 41–92, [arXiv:1002.2206](https://arxiv.org/abs/1002.2206) [hep-ph].
- [2] K. M. Burke, A. Buzzatti, N. Chang, C. Gale, M. Gyulassy, *et al.*, “Extracting jet transport coefficient from jet quenching at RHIC and LHC,” *Phys.Rev.* **C90** (2014) 014909, [arXiv:1312.5003](https://arxiv.org/abs/1312.5003) [nucl-th].
- [3] F. D’Eramo, M. Lekaveckas, H. Liu, and K. Rajagopal, “Momentum Broadening in Weakly Coupled Quark-Gluon Plasma (with a view to finding the quasiparticles within liquid quark-gluon plasma),” *JHEP* **05** (2013) 031, [arXiv:1211.1922](https://arxiv.org/abs/1211.1922) [hep-ph].
- [4] **PHENIX** Collaboration, K. Adcox *et al.*, “Suppression of hadrons with large transverse momentum in central Au+Au collisions at $\sqrt{s_{NN}} = 130\text{-GeV}$,” *Phys.Rev.Lett.* **88** (2002) 022301, [arXiv:nucl-ex/0109003](https://arxiv.org/abs/nucl-ex/0109003) [nucl-ex].
- [5] **PHENIX** Collaboration, A. Adare *et al.*, “Neutral pion production with respect to centrality and reaction plane in Au+Au collisions at $\sqrt{s_{NN}}=200\text{ GeV}$,” *Phys.Rev.* **C87** (2013) 034911, [arXiv:1208.2254](https://arxiv.org/abs/1208.2254) [nucl-ex].
- [6] **PHENIX** Collaboration, A. Adare *et al.*, “Trends in Yield and Azimuthal Shape Modification in Dihadron Correlations in Relativistic Heavy Ion Collisions,” *Phys.Rev.Lett.* **104** (2010) 252301, [arXiv:1002.1077](https://arxiv.org/abs/1002.1077) [nucl-ex].

[7] **STAR** Collaboration, C. Adler *et al.*, “Centrality dependence of high p_T hadron suppression in Au+Au collisions at $\sqrt{s_{NN}} = 130$ –GeV,” *Phys.Rev.Lett.* **89** (2002) 202301, arXiv:nucl-ex/0206011 [nucl-ex].

[8] **STAR** Collaboration, C. Adler *et al.*, “Disappearance of back-to-back high p_T hadron correlations in central Au+Au collisions at $\sqrt{s_{NN}} = 200$ GeV,” *Phys.Rev.Lett.* **90** (2003) 082302, arXiv:nucl-ex/0210033 [nucl-ex].

[9] **STAR** Collaboration, J. Adams *et al.*, “Transverse momentum and collision energy dependence of high p_T hadron suppression in Au+Au collisions at ultrarelativistic energies,” *Phys.Rev.Lett.* **91** (2003) 172302, arXiv:nucl-ex/0305015 [nucl-ex].

[10] **STAR** Collaboration, J. Adams *et al.*, “Direct observation of dijets in central Au + Au collisions at $\sqrt{s_{NN}} = 200$ GeV,” *Phys. Rev. Lett.* **97** (2006) 162301, arXiv:nucl-ex/0604018.

[11] **STAR** Collaboration, L. Adamczyk *et al.*, “Jet-Hadron Correlations in $\sqrt{s_{NN}} = 200$ GeV $p + p$ and Central Au + Au Collisions,” *Phys.Rev.Lett.* **112** (2014) 122301, arXiv:1302.6184 [nucl-ex].

[12] **PHENIX** Collaboration, A. Adare *et al.*, “Medium modification of jet fragmentation in Au + Au collisions at $\sqrt{s_{NN}} = 200$ GeV measured in direct photon-hadron correlations,” *Phys.Rev.Lett.* **111** (2013) 032301, arXiv:1212.3323 [nucl-ex].

[13] **ALICE** Collaboration, B. Abelev *et al.*, “Centrality Dependence of Charged Particle Production at Large Transverse Momentum in Pb–Pb Collisions at $\sqrt{s_{NN}} = 2.76$ TeV,” *Phys.Lett.* **B720** (2013) 52–62, arXiv:1208.2711 [hep-ex].

[14] **CMS** Collaboration, S. Chatrchyan *et al.*, “Study of high- p_T charged particle suppression in PbPb compared to pp collisions at $\sqrt{s_{NN}} = 2.76$ TeV,” *Eur.Phys.J.* **C72** (2012) 1945, arXiv:1202.2554 [nucl-ex].

[15] **ALICE** Collaboration, K. Aamodt *et al.*, “Particle-yield modification in jet-like azimuthal di-hadron correlations in Pb–Pb collisions at $\sqrt{s_{NN}} = 2.76$ TeV,” *Phys.Rev.Lett.* **108** (2012) 092301, arXiv:1110.0121 [nucl-ex].

[16] **CMS** Collaboration, S. Chatrchyan *et al.*, “Centrality dependence of dihadron correlations and azimuthal anisotropy harmonics in PbPb collisions at $\sqrt{s_{NN}} = 2.76$ TeV,” *Eur.Phys.J.* **C72** (2012) 10052, arXiv:1201.3158 [nucl-ex].

[17] **ALICE** Collaboration, B. Abelev *et al.*, “Measurement of charged jet suppression in Pb–Pb collisions at $\sqrt{s_{NN}} = 2.76$ TeV,” *JHEP* **03** (2014) 013, arXiv:1311.0633 [nucl-ex].

[18] **ATLAS** Collaboration, G. Aad *et al.*, “Measurements of the Nuclear Modification Factor for Jets in Pb+Pb Collisions at $\sqrt{s_{NN}} = 2.76$ TeV with the ATLAS Detector,” arXiv:1411.2357 [hep-ex].

[19] **CMS** Collaboration, S. Chatrchyan *et al.*, “Nuclear modification factor of high transverse momentum jets in PbPb collisions at $\sqrt{s_{NN}} = 2.76$ TeV,” *CMS-PAS-HIN-12-004* (2012) .

[20] **ALICE** Collaboration, J. Adam *et al.*, “Measurement of jet suppression in central Pb–Pb collisions at $\sqrt{s_{NN}} = 2.76$ TeV,” *Phys.Lett.* **B746** (2015) 1–14, arXiv:1502.01689 [nucl-ex].

[21] **CMS** Collaboration, S. Chatrchyan *et al.*, “Jet momentum dependence of jet quenching in PbPb collisions at $\sqrt{s_{NN}} = 2.76$ TeV,” *Phys.Lett.* **B712** (2012) 176–197, arXiv:1202.5022 [nucl-ex].

[22] **ATLAS** Collaboration, G. Aad *et al.*, “Observation of a Centrality-Dependent Dijet Asymmetry in Lead-Lead Collisions at $\sqrt{s_{NN}} = 2.76$ TeV with the ATLAS Detector at the LHC,” *Phys.Rev.Lett.* **105** (2010) 252303, arXiv:1011.6182 [hep-ex].

[23] **CMS** Collaboration, S. Chatrchyan *et al.*, “Observation and studies of jet quenching in PbPb collisions at nucleon-nucleon center-of-mass energy = 2.76 TeV,” *Phys.Rev.* **C84** (2011) 024906, arXiv:1102.1957 [nucl-ex].

[24] M. Cacciari, G. P. Salam, and G. Soyez, “FastJet User Manual,” *Eur.Phys.J.* **C72** (2012) 1896,

arXiv:1111.6097 [hep-ph].

[25] M. Cacciari, G. P. Salam, and G. Soyez, “The anti- k_t jet clustering algorithm,” *JHEP* **04** (2008) 063, arXiv:0802.1189 [hep-ph].

[26] T. Sjöstrand, S. Mrenna, and P. Z. Skands, “PYTHIA 6.4 Physics and Manual,” *JHEP* **05** (2006) 026, arXiv:hep-ph/0603175 [hep-ph].

[27] D. de Florian, “Next-to-leading order QCD corrections to hadron+jet production in pp collisions at RHIC,” *Phys.Rev.* **D79** (2009) 114014, arXiv:0904.4402 [hep-ph].

[28] X.-N. Wang and Y. Zhu, “Medium Modification of γ -jets in High-energy Heavy-ion Collisions,” *Phys.Rev.Lett.* **111** (2013) 062301, arXiv:1302.5874 [hep-ph].

[29] ALICE Collaboration, K. Aamodt *et al.*, “The ALICE experiment at the CERN LHC,” *JINST* **3** (2008) S08002.

[30] ALICE Collaboration, B. Abelev *et al.*, “Performance of the ALICE Experiment at the CERN LHC,” *Int.J.Mod.Phys.* **A29** (2014) 1430044, arXiv:1402.4476 [nucl-ex].

[31] ALICE Collaboration, B. Abelev *et al.*, “Charged jet cross sections and properties in proton-proton collisions at $\sqrt{s} = 7$ TeV,” arXiv:1411.4969 [nucl-ex].

[32] P. Z. Skands, “Tuning Monte Carlo Generators: The Perugia Tunes,” *Phys.Rev.* **D82** (2010) 074018, arXiv:1005.3457 [hep-ph].

[33] R. Brun, F. Bruyant, M. Maire, A.C. McPherson, and P. Zanarini, “GEANT3 User’s Guide,” *CERN Data Handling Division DD/EE/84-1* (1985) .

[34] X.-N. Wang and M. Gyulassy, “HIJING: A Monte Carlo model for multiple jet production in p p, p A and A A collisions,” *Phys.Rev.* **D44** (1991) 3501–3516.

[35] M. Cacciari, G. P. Salam, and G. Soyez, “The Catchment Area of Jets,” *JHEP* **04** (2008) 005, arXiv:0802.1188 [hep-ph].

[36] H.-M. Chang, M. Procura, J. Thaler, and W. J. Waalewijn, “Calculating Track-Based Observables for the LHC,” *Phys.Rev.Lett.* **111** (2013) 102002, arXiv:1303.6637 [hep-ph].

[37] M. Cacciari and G. P. Salam, “Pileup subtraction using jet areas,” *Phys. Lett.* **B659** (2008) 119–126, arXiv:0707.1378 [hep-ph].

[38] ALICE Collaboration, B. Abelev *et al.*, “Measurement of Event Background Fluctuations for Charged Particle Jet Reconstruction in Pb-Pb collisions at $\sqrt{s_{NN}} = 2.76$ TeV,” *JHEP* **03** (2012) 053, arXiv:1201.2423 [hep-ex].

[39] G. de Barros, “Inclusive Distribution of Fully Reconstructed Jets in Heavy Ion Collisions at RHIC: Status Report,” *AIP Conf.Proc.* **1441** (2012) 825–828, arXiv:1109.4386 [hep-ex].

[40] STAR Collaboration, P. Jacobs, “Background Fluctuations in Heavy Ion Jet Reconstruction,” arXiv:1012.2406 [nucl-ex].

[41] O. Kodolova, I. Vardanian, A. Nikitenko, and A. Oulianov, “The performance of the jet identification and reconstruction in heavy ions collisions with CMS detector,” *Eur.Phys.J.* **C50** (2007) 117–123.

[42] ATLAS Collaboration, G. Aad *et al.*, “Measurement of the jet radius and transverse momentum dependence of inclusive jet suppression in lead-lead collisions at $\sqrt{s_{NN}} = 2.76$ TeV with the ATLAS detector,” *Phys.Lett.* **B719** (2013) 220–241, arXiv:1208.1967 [hep-ex].

[43] CMS Collaboration, S. Chatrchyan *et al.*, “Studies of jet quenching using isolated-photon+jet correlations in PbPb and pp collisions at $\sqrt{s_{NN}} = 2.76$ TeV,” *Phys.Lett.* **B718** (2013) 773–794, arXiv:1205.0206 [nucl-ex].

[44] T. Renk, H. Holopainen, R. Paatelainen, and K. J. Eskola, “Systematics of the charged-hadron p_T spectrum and the nuclear suppression factor in heavy-ion collisions from $\sqrt{s} = 200$ GeV to $\sqrt{s} = 2.76$ TeV,” *Phys.Rev.* **C84** (2011) 014906, arXiv:1103.5308 [hep-ph].

[45] D. d’Enterria, K. J. Eskola, I. Helenius, and H. Paukkunen, “Confronting current NLO parton

fragmentation functions with inclusive charged-particle spectra at hadron colliders,” *Nucl.Phys.* **B883** (2014) 615–628, arXiv:1311.1415 [hep-ph].

[46] N. Armesto, L. Cunqueiro, C. A. Salgado, and W.-C. Xiang, “Medium-evolved fragmentation functions,” *JHEP* **02** (2008) 048, arXiv:0710.3073 [hep-ph].

[47] N.-B. Chang, W.-T. Deng, and X.-N. Wang, “Initial Conditions for Modified DGLAP Evolution of the Modified Fragmentation Functions in Nuclear Medium,” *Phys.Rev.* **C89** (2014) 034911, arXiv:1401.5109 [nucl-th].

[48] ALICE Collaboration, B. Alessandro *et al.*, “ALICE: Physics performance report, volume II,” *J.Phys.* **G32** (2006) 1295–2040.

[49] R. Baier, “Jet quenching,” *Nucl.Phys.* **A715** (2003) 209–218, arXiv:hep-ph/0209038 [hep-ph].

[50] A. Drees, H. Feng, and J. Jia, “Medium induced jet absorption at RHIC,” *Phys.Rev.* **C71** (2005) 034909, arXiv:nucl-th/0310044 [nucl-th].

[51] A. Dainese, C. Loizides, and G. Paic, “Leading-particle suppression in high energy nucleus-nucleus collisions,” *Eur.Phys.J.* **C38** (2005) 461–474, arXiv:hep-ph/0406201 [hep-ph].

[52] K. Eskola, H. Honkanen, C. Salgado, and U. Wiedemann, “The Fragility of high- p_T hadron spectra as a hard probe,” *Nucl.Phys.* **A747** (2005) 511–529, arXiv:hep-ph/0406319 [hep-ph].

[53] T. Renk, “Through the blackness - high- p_T hadrons probing the central region of 200A GeV Au-Au collisions,” *Phys.Rev.* **C74** (2006) 024903, arXiv:hep-ph/0602045 [hep-ph].

[54] C. Loizides, “High transverse momentum suppression and surface effects in Cu+Cu and Au+Au collisions within the PQM model,” *Eur.Phys.J.* **C49** (2007) 339–345, arXiv:hep-ph/0608133 [hep-ph].

[55] H. Zhang, J. Owens, E. Wang, and X.-N. Wang, “Dihadron tomography of high-energy nuclear collisions in NLO pQCD,” *Phys.Rev.Lett.* **98** (2007) 212301, arXiv:nucl-th/0701045 [nucl-th].

[56] T. Renk, “Energy dependence of the dijet imbalance in Pb-Pb collisions at 2.76 ATeV,” *Phys.Rev.* **C86** (2012) 061901, arXiv:1204.5572 [hep-ph].

[57] G. de Barros, B. Fenton-Olsen, P. Jacobs, and M. Ploskon, “Data-driven analysis methods for the measurement of reconstructed jets in heavy ion collisions at RHIC and LHC,” *Nucl.Phys.* **A910-911** (2013) 314–318, arXiv:1208.1518 [hep-ex].

[58] G. Cowan, “A survey of unfolding methods for particle physics,” *Conf.Proc.* **C0203181** (2002) 248–257.

[59] A. Höcker and V. Kartvelishvili, “SVD approach to data unfolding,” *Nucl.Instrum.Meth.* **A372** (1996) 469–481, arXiv:hep-ph/9509307 [hep-ph].

[60] G. D’Agostini, “A multidimensional unfolding method based on Bayes’ theorem,” *Nucl.Instrum.Meth.* **A362** (1995) 487–498.

[61] RooUnfold <http://hepunx.rl.ac.uk/~adye/software/unfold/RooUnfold.html>.

[62] CMS Collaboration, S. Chatrchyan *et al.*, “Azimuthal anisotropy of charged particles at high transverse momenta in PbPb collisions at $\sqrt{s_{NN}} = 2.76$ TeV,” *Phys.Rev.Lett.* **109** (2012) 022301, arXiv:1204.1850 [nucl-ex].

[63] ALICE Collaboration, B. Abelev *et al.*, “Anisotropic flow of charged hadrons, pions and (anti-)protons measured at high transverse momentum in Pb-Pb collisions at $\sqrt{s_{NN}}=2.76$ TeV,” *Phys.Lett.* **B719** (2013) 18–28, arXiv:1205.5761 [nucl-ex].

[64] I. Lokhtin, A. Belyaev, and A. Snigirev, “Jet quenching pattern at lhc in pyquen model,” *Eur.Phys.J.* **C71** (2011) 1650, arXiv:1103.1853 [hep-ph].

[65] D. de Florian, R. Sassot, and M. Stratmann, “Global analysis of fragmentation functions for

protons and charged hadrons,” *Phys.Rev.* **D76** (2007) 074033, [arXiv:0707.1506 \[hep-ph\]](https://arxiv.org/abs/0707.1506).

[66] H.-L. Lai, M. Guzzi, J. Huston, Z. Li, P. M. Nadolsky, *et al.*, “New parton distributions for collider physics,” *Phys.Rev.* **D82** (2010) 074024, [arXiv:1007.2241 \[hep-ph\]](https://arxiv.org/abs/1007.2241).

[67] M. Dasgupta, L. Magnea, and G. P. Salam, “Non-perturbative QCD effects in jets at hadron colliders,” *JHEP* **02** (2008) 055, [arXiv:0712.3014 \[hep-ph\]](https://arxiv.org/abs/0712.3014).

[68] G. Soyez, “A simple description of jet cross-section ratios,” *Phys.Lett.* **B698** (2011) 59–62, [arXiv:1101.2665 \[hep-ph\]](https://arxiv.org/abs/1101.2665).

[69] M. Dasgupta, F. Dreyer, G. P. Salam, and G. Soyez, “Small-radius jets to all orders in QCD,” [arXiv:1411.5182 \[hep-ph\]](https://arxiv.org/abs/1411.5182).

[70] **ALICE** Collaboration, B. Abelev *et al.*, “Measurement of the inclusive differential jet cross section in pp collisions at $\sqrt{s} = 2.76$ TeV,” *Phys.Lett.* **B722** (2013) 262–272, [arXiv:1301.3475 \[nucl-ex\]](https://arxiv.org/abs/1301.3475).

[71] A. Kurkela and U. A. Wiedemann, “Picturing perturbative parton cascades in QCD matter,” [arXiv:1407.0293 \[hep-ph\]](https://arxiv.org/abs/1407.0293).

[72] **CMS** Collaboration, S. Chatrchyan *et al.*, “Modification of jet shapes in PbPb collisions at $\sqrt{s_{NN}} = 2.76$ TeV,” *Phys.Lett.* **B730** (2014) 243–263, [arXiv:1310.0878 \[nucl-ex\]](https://arxiv.org/abs/1310.0878).

A The ALICE Collaboration

J. Adam⁴⁰, D. Adamová⁸³, M.M. Aggarwal⁸⁷, G. Aglieri Rinella³⁶, M. Agnello¹¹¹, N. Agrawal⁴⁸, Z. Ahammed¹³², S.U. Ahn⁶⁸, I. Aimo^{94,111}, S. Aiola¹³⁷, M. Ajaz¹⁶, A. Akindinov⁵⁸, S.N. Alam¹³², D. Aleksandrov¹⁰⁰, B. Alessandro¹¹¹, D. Alexandre¹⁰², R. Alfaro Molina⁶⁴, A. Alici^{105,12}, A. Alkin³, J.R.M. Almaraz¹¹⁹, J. Alme³⁸, T. Alt⁴³, S. Altinpinar¹⁸, I. Altsybeev¹³¹, C. Alves Garcia Prado¹²⁰, C. Andrei⁷⁸, A. Andronic⁹⁷, V. Anguelov⁹³, J. Anielski⁵⁴, T. Antičić⁹⁸, F. Antinori¹⁰⁸, P. Antonioli¹⁰⁵, L. Aphecetche¹¹³, H. Appelshäuser⁵³, S. Arcelli²⁸, N. Armesto¹⁷, R. Arnaldi¹¹¹, I.C. Arsene²², M. Arslanbekov⁵³, B. Audurier¹¹³, A. Augustinus³⁶, R. Averbeck⁹⁷, M.D. Azmi¹⁹, M. Bach⁴³, A. Badalà¹⁰⁷, Y.W. Baek⁴⁴, S. Bagnasco¹¹¹, R. Bailhache⁵³, R. Bala⁹⁰, A. Baldissari¹⁵, F. Baltasar Dos Santos Pedrosa³⁶, R.C. Baral⁶¹, A.M. Barbano¹¹¹, R. Barbera²⁹, F. Barile³³, G.G. Barnaföldi¹³⁶, L.S. Barnby¹⁰², V. Barret⁷⁰, P. Bartalini⁷, K. Barth³⁶, J. Bartke¹¹⁷, E. Bartsch⁵³, M. Basile²⁸, N. Bastid⁷⁰, S. Basu¹³², B. Bathen⁵⁴, G. Batigne¹¹³, A. Batista Camejo⁷⁰, B. Batyunya⁶⁶, P.C. Batzing²², I.G. Bearden⁸⁰, H. Beck⁵³, C. Bedda¹¹¹, N.K. Behera^{49,48}, I. Belikov⁵⁵, F. Bellini²⁸, H. Bello Martinez², R. Bellwied¹²², R. Belmont¹³⁵, E. Belmont-Moreno⁶⁴, V. Belyaev⁷⁶, G. Bencedi¹³⁶, S. Beole²⁷, I. Berceanu⁷⁸, A. Bercuci⁷⁸, Y. Berdnikov⁸⁵, D. Berenyi¹³⁶, R.A. Bertens⁵⁷, D. Berzana^{36,27}, L. Betev³⁶, A. Bhasin⁹⁰, I.R. Bhat⁹⁰, A.K. Bhati⁸⁷, B. Bhattacharjee⁴⁵, J. Bhom¹²⁸, L. Bianchi¹²², N. Bianchi⁷², C. Bianchin^{135,57}, J. Bielčík⁴⁰, J. Bielčíková⁸³, A. Bilandzic⁸⁰, R. Biswas⁴, S. Biswas⁷⁹, S. Bjelogrlic⁵⁷, F. Blanco¹⁰, D. Blau¹⁰⁰, C. Blume⁵³, F. Bock^{74,93}, A. Bogdanov⁷⁶, H. Bøggild⁸⁰, L. Boldizsár¹³⁶, M. Bombara⁴¹, J. Book⁵³, H. Borel¹⁵, A. Borissov⁹⁶, M. Borri⁸², F. Bossú⁶⁵, E. Botta²⁷, S. Böttger⁵², P. Braun-Munzinger⁹⁷, M. Bregant¹²⁰, T. Breitner⁵², T.A. Broker⁵³, T.A. Browning⁹⁵, M. Broz⁴⁰, E.J. Brucken⁴⁶, E. Bruna¹¹¹, G.E. Bruno³³, D. Budnikov⁹⁹, H. Buesching⁵³, S. Bufalino^{111,36}, P. Buncic³⁶, O. Busch^{93,128}, Z. Buthelezi⁶⁵, J.B. Butt¹⁶, J.T. Buxton²⁰, D. Caffarri³⁶, X. Cai⁷, H. Caines¹³⁷, L. Calero Diaz⁷², A. Caliva⁵⁷, E. Calvo Villar¹⁰³, P. Camerini²⁶, F. Carena³⁶, W. Carena³⁶, J. Castillo Castellanos¹⁵, A.J. Castro¹²⁵, E.A.R. Casula²⁵, C. Cavicchioli³⁶, C. Ceballos Sanchez⁹, J. Cepila⁴⁰, P. Cerello¹¹¹, J. Cerkala¹¹⁵, B. Chang¹²³, S. Chapeland³⁶, M. Chartier¹²⁴, J.L. Charvet¹⁵, S. Chattopadhyay¹³², S. Chattopadhyay¹⁰¹, V. Chelnokov³, M. Cherney⁸⁶, C. Cheshkov¹³⁰, B. Cheynis¹³⁰, V. Chibante Barroso³⁶, D.D. Chinellato¹²¹, P. Chochula³⁶, K. Choi⁹⁶, M. Chojnacki⁸⁰, S. Choudhury¹³², P. Christakoglou⁸¹, C.H. Christensen⁸⁰, P. Christiansen³⁴, T. Chujo¹²⁸, S.U. Chung⁹⁶, Z. Chunhui⁵⁷, C. Cicalo¹⁰⁶, L. Cifarelli^{12,28}, F. Cindolo¹⁰⁵, J. Cleymans⁸⁹, F. Colamaria³³, D. Colella^{36,59,33}, A. Collu²⁵, M. Colocci²⁸, G. Conesa Balbastre⁷¹, Z. Conesa del Valle⁵¹, M.E. Connors¹³⁷, J.G. Contreras^{11,40}, T.M. Cormier⁸⁴, Y. Corrales Morales²⁷, I. Cortés Maldonado², P. Cortese³², M.R. Cosentino¹²⁰, F. Costa³⁶, P. Crochet⁷⁰, R. Cruz Albino¹¹, E. Cuautle⁶³, L. Cunqueiro³⁶, T. Dahms^{92,37}, A. Dainese¹⁰⁸, A. Danu⁶², D. Das¹⁰¹, I. Das^{51,101}, S. Das⁴, A. Dash¹²¹, S. Dash⁴⁸, S. De¹²⁰, A. De Caro^{31,12}, G. de Cataldo¹⁰⁴, J. de Cuveland⁴³, A. De Falco²⁵, D. De Gruttola^{12,31}, N. De Marco¹¹¹, S. De Pasquale³¹, A. Deisting^{97,93}, A. Deloff⁷⁷, E. Dénes¹³⁶, G. D'Erasmo³³, D. Di Bari³³, A. Di Mauro³⁶, P. Di Nezza⁷², M.A. Diaz Corchero¹⁰, T. Dietel⁸⁹, P. Dillenseger⁵³, R. Divià³⁶, Ø. Djupsland¹⁸, A. Dobrin^{57,81}, T. Dobrowolski^{77,1}, D. Domenicis Gimenez¹²⁰, B. Dönigus⁵³, O. Dordic²², A.K. Dubey¹³², A. Dubla⁵⁷, L. Ducrour¹³⁰, P. Dupieux⁷⁰, R.J. Ehlers¹³⁷, D. Elia¹⁰⁴, H. Engel⁵², B. Erazmus^{36,113}, I. Erdemir⁵³, F. Erhardt¹²⁹, D. Eschweiler⁴³, B. Espagnon⁵¹, M. Estienne¹¹³, S. Esumi¹²⁸, J. Eum⁹⁶, D. Evans¹⁰², S. Evdokimov¹¹², G. Eyyubova⁴⁰, L. Fabbietti^{37,92}, D. Fabris¹⁰⁸, J. Faivre⁷¹, A. Fantoni⁷², M. Fasel⁷⁴, L. Feldkamp⁵⁴, D. Felea⁶², A. Feliciello¹¹¹, G. Feofilov¹³¹, J. Ferencei⁸³, A. Fernández Téllez², E.G. Ferreiro¹⁷, A. Ferretti²⁷, A. Festanti³⁰, V.J.G. Feuillard^{70,15}, J. Figiel¹¹⁷, M.A.S. Figueiredo¹²⁴, S. Filchagin⁹⁹, D. Finogeev⁵⁶, E.M. Fiore³³, M.G. Fleck⁹³, M. Floris³⁶, S. Foertsch⁶⁵, P. Foka⁹⁷, S. Fokin¹⁰⁰, E. Fragiocomo¹¹⁰, A. Francescon^{36,30}, U. Frankenfeld⁹⁷, U. Fuchs³⁶, C. Furget⁷¹, A. Furs⁵⁶, M. Fusco Girard³¹, J.J. Gaardhøje⁸⁰, M. Gagliardi²⁷, A.M. Gago¹⁰³, M. Gallio²⁷, D.R. Gangadharan⁷⁴, P. Ganoti⁸⁸, C. Gao⁷, C. Garabatos⁹⁷, E. Garcia-Solis¹³, C. Gargiulo³⁶, P. Gasik^{92,37}, M. Germain¹¹³, A. Gheata³⁶, M. Gheata^{62,36}, P. Ghosh¹³², S.K. Ghosh⁴, P. Gianotti⁷², P. Giubellino³⁶, P. Giubilato³⁰, E. Gladysz-Dziadus¹¹⁷, P. Glässel⁹³, A. Gomez Ramirez⁵², P. González-Zamora¹⁰, S. Gorbunov⁴³, L. Görlich¹¹⁷, S. Gotovac¹¹⁶, V. Grabski⁶⁴, L.K. Graczykowski¹³⁴, K.L. Graham¹⁰², A. Grelli⁵⁷, A. Grigoras³⁶, C. Grigoras³⁶, V. Grigoriev⁷⁶, A. Grigoryan¹, S. Grigoryan⁶⁶, B. Grinyov³, N. Grion¹¹⁰, J.F. Grosse-Oetringhaus³⁶, J.-Y. Grossiord¹³⁰, R. Grossiord³⁶, F. Guber⁵⁶, R. Guernane⁷¹, B. Guerzoni²⁸, K. Gulbrandsen⁸⁰, H. Gulkanyan¹, T. Gunji¹²⁷, A. Gupta⁹⁰, R. Gupta⁹⁰, R. Haake⁵⁴, Ø. Haaland¹⁸, C. Hadjidakis⁵¹, M. Haiduc⁶², H. Hamagaki¹²⁷, G. Hamar¹³⁶, A. Hansen⁸⁰, J.W. Harris¹³⁷, H. Hartmann⁴³, A. Harton¹³, D. Hatzifotiadou¹⁰⁵, S. Hayashi¹²⁷, S.T. Heckel⁵³, M. Heide⁵⁴, H. Helstrup³⁸, A. Herghelegiu⁷⁸, G. Herrera Corral¹¹, B.A. Hess³⁵, K.F. Hetland³⁸, T.E. Hilden⁴⁶, H. Hillemanns³⁶, B. Hippolyte⁵⁵, R. Hosokawa¹²⁸, P. Hristov³⁶, M. Huang¹⁸, T.J. Humanic²⁰, N. Hussain⁴⁵, T. Hussain¹⁹, D. Hutter⁴³, D.S. Hwang²¹, R. Ilkaev⁹⁹, I. Ilkiv⁷⁷, M. Inaba¹²⁸, M. Ippolitov^{76,100}, M. Irfan¹⁹, M. Ivanov⁹⁷, V. Ivanov⁸⁵, V. Izucheev¹¹², P.M. Jacobs⁷⁴, S. Jadlovska¹¹⁵,

C. Jahnke¹²⁰, H.J. Jang⁶⁸, M.A. Janik¹³⁴, P.H.S.Y. Jayarathna¹²², C. Jena³⁰, S. Jena¹²², R.T. Jimenez Bustamante⁹⁷, P.G. Jones¹⁰², H. Jung⁴⁴, A. Jusko¹⁰², P. Kalinak⁵⁹, A. Kalweit³⁶, J. Kamin⁵³, J.H. Kang¹³⁸, V. Kaplin⁷⁶, S. Kar¹³², A. Karasu Uysal⁶⁹, O. Karavichev⁵⁶, T. Karavicheva⁵⁶, L. Karayan^{93,97}, E. Karpechev⁵⁶, U. Kebischull⁵², R. Keidel¹³⁹, D.L.D. Keijdener⁵⁷, M. Keil³⁶, K.H. Khan¹⁶, M.M. Khan¹⁹, P. Khan¹⁰¹, S.A. Khan¹³², A. Khanzadeev⁸⁵, Y. Kharlov¹¹², B. Kileng³⁸, B. Kim¹³⁸, D.W. Kim^{44,68}, D.J. Kim¹²³, H. Kim¹³⁸, J.S. Kim⁴⁴, M. Kim⁴⁴, M. Kim¹³⁸, S. Kim²¹, T. Kim¹³⁸, S. Kirsch⁴³, I. Kisel⁴³, S. Kiselev⁵⁸, A. Kisiel¹³⁴, G. Kiss¹³⁶, J.L. Klay⁶, C. Klein⁵³, J. Klein^{36,93}, C. Klein-Bösing⁵⁴, A. Kluge³⁶, M.L. Knichel⁹³, A.G. Knospe¹¹⁸, T. Kobayashi¹²⁸, C. Kobdaj¹¹⁴, M. Kofarago³⁶, T. Kollegger^{97,43}, A. Kolojvari¹³¹, V. Kondratiev¹³¹, N. Kondratyeva⁷⁶, E. Kondratyuk¹¹², A. Konevskikh⁵⁶, M. Kopcik¹¹⁵, M. Kour⁹⁰, C. Kouzinopoulos³⁶, O. Kovalenko⁷⁷, V. Kovalenko¹³¹, M. Kowalski¹¹⁷, G. Koyithatta Meethaleveedu⁴⁸, J. Kral¹²³, I. Králik⁵⁹, A. Kravčáková⁴¹, M. Krelina⁴⁰, M. Kretz⁴³, M. Krivda^{102,59}, F. Krizek⁸³, E. Kryshen³⁶, M. Krzewicki⁴³, A.M. Kubera²⁰, V. Kučera⁸³, T. Kugathasan³⁶, C. Kuhn⁵⁵, P.G. Kuijer⁸¹, I. Kulakov⁴³, A. Kumar⁹⁰, J. Kumar⁴⁸, L. Kumar^{79,87}, P. Kurashvili⁷⁷, A. Kurepin⁵⁶, A.B. Kurepin⁵⁶, A. Kuryakin⁹⁹, S. Kushpil⁸³, M.J. Kweon⁵⁰, Y. Kwon¹³⁸, S.L. La Pointe¹¹¹, P. La Rocca²⁹, C. Lagana Fernandes¹²⁰, I. Lakomov³⁶, R. Langoy⁴², C. Lara⁵², A. Lardeux¹⁵, A. Lattuca²⁷, E. Laudi³⁶, R. Lea²⁶, L. Leardini⁹³, G.R. Lee¹⁰², S. Lee¹³⁸, I. Legrand³⁶, F. Lehas⁸¹, R.C. Lemmon⁸², V. Lenti¹⁰⁴, E. Leogrande⁵⁷, I. León Monzón¹¹⁹, M. Leoncino²⁷, P. Lévai¹³⁶, S. Li^{70,7}, X. Li¹⁴, J. Lien⁴², R. Lietava¹⁰², S. Lindal²², V. Lindenstruth⁴³, C. Lippmann⁹⁷, M.A. Lisa²⁰, H.M. Ljunggren³⁴, D.F. Lodato⁵⁷, P.I. Loenne¹⁸, V. Loginov⁷⁶, C. Loizides⁷⁴, X. Lopez⁷⁰, E. López Torres⁹, A. Lowe¹³⁶, P. Luettig⁵³, M. Lunardon³⁰, G. Luparello²⁶, P.H.F.N.D. Luz¹²⁰, R. Ma¹³⁷, A. Maevskaia⁵⁶, M. Mager³⁶, S. Mahajan⁹⁰, S.M. Mahmood²², A. Maire⁵⁵, R.D. Majka¹³⁷, M. Malaev⁸⁵, I. Maldonado Cervantes⁶³, L. Malinina^{ii,66}, D. Mal'Kevich⁵⁸, P. Malzacher⁹⁷, A. Mamontov⁹⁹, V. Manko¹⁰⁰, F. Manso⁷⁰, V. Manzari^{36,104}, M. Marchisone²⁷, J. Mareš⁶⁰, G.V. Margagliotti²⁶, A. Margotti¹⁰⁵, J. Margutti⁵⁷, A. Marín⁹⁷, C. Markert¹¹⁸, M. Marquard⁵³, N.A. Martin⁹⁷, J. Martin Blanco¹¹³, P. Martinengo³⁶, M.I. Martínez², G. Martínez García¹¹³, M. Martinez Pedreira³⁶, Y. Martynov³, A. Mas¹²⁰, S. Masciocchi⁹⁷, M. Masera²⁷, A. Masoni¹⁰⁶, L. Massacrier¹¹³, A. Mastroserio³³, H. Masui¹²⁸, A. Matyja¹¹⁷, C. Mayer¹¹⁷, J. Mazer¹²⁵, M.A. Mazzoni¹⁰⁹, D. McDonald¹²², F. Meddi²⁴, Y. Melikyan⁷⁶, A. Menchaca-Rocha⁶⁴, E. Meninno³¹, J. Mercado Pérez⁹³, M. Meres³⁹, Y. Miake¹²⁸, M.M. Mieskolainen⁴⁶, K. Mikhaylov^{66,58}, L. Milano³⁶, J. Milosevic^{22,133}, L.M. Minervini^{104,23}, A. Mischke⁵⁷, A.N. Mishra⁴⁹, D. Miškowiec⁹⁷, J. Mitra¹³², C.M. Mitu⁶², N. Mohammadi⁵⁷, B. Mohanty^{132,79}, L. Molnar⁵⁵, L. Montaño Zetina¹¹, E. Montes¹⁰, M. Morando³⁰, D.A. Moreira De Godoy^{113,54}, S. Moretto³⁰, A. Morreale¹¹³, A. Morsch³⁶, V. Muccifora⁷², E. Mudnic¹¹⁶, D. Mühlheim⁵⁴, S. Muhuri¹³², M. Mukherjee¹³², J.D. Mulligan¹³⁷, M.G. Munhoz¹²⁰, S. Murray⁶⁵, L. Musa³⁶, J. Musinsky⁵⁹, B.K. Nandi⁴⁸, R. Nania¹⁰⁵, E. Nappi¹⁰⁴, M.U. Naru¹⁶, C. Nattrass¹²⁵, K. Nayak⁷⁹, T.K. Nayak¹³², S. Nazarenko⁹⁹, A. Nedosekin⁵⁸, L. Nellen⁶³, F. Ng¹²², M. Nicassio⁹⁷, M. Niculescu^{62,36}, J. Niedziela³⁶, B.S. Nielsen⁸⁰, S. Nikolaev¹⁰⁰, S. Nikulin¹⁰⁰, V. Nikulin⁸⁵, F. Noferini^{105,12}, P. Nomokonov⁶⁶, G. Nooren⁵⁷, J.C.C. Noris², J. Norman¹²⁴, A. Nyanin¹⁰⁰, J. Nystrand¹⁸, H. Oeschler⁹³, S. Oh¹³⁷, S.K. Oh⁶⁷, A. Ohlson³⁶, A. Okatan⁶⁹, T. Okubo⁴⁷, L. Olah¹³⁶, J. Oleniacz¹³⁴, A.C. Oliveira Da Silva¹²⁰, M.H. Oliver¹³⁷, J. Onderwaater⁹⁷, C. Oppedisano¹¹¹, R. Orava⁴⁶, A. Ortiz Velasquez⁶³, A. Oskarsson³⁴, J. Otwinowski¹¹⁷, K. Oyama⁹³, M. Ozdemir⁵³, Y. Pachmayer⁹³, P. Pagano³¹, G. Paić⁶³, C. Pajares¹⁷, S.K. Pal¹³², J. Pan¹³⁵, A.K. Pandey⁴⁸, D. Pant⁴⁸, P. Papcun¹¹⁵, V. Papikyan¹, G.S. Pappalardo¹⁰⁷, P. Pareek⁴⁹, W.J. Park⁹⁷, S. Parmar⁸⁷, A. Passfeld⁵⁴, V. Paticchio¹⁰⁴, R.N. Patra¹³², B. Paul¹⁰¹, T. Peitzmann⁵⁷, H. Pereira Da Costa¹⁵, E. Pereira De Oliveira Filho¹²⁰, D. Peresunko^{100,76}, C.E. Pérez Lara⁸¹, E. Perez Lezama^{53,43}, V. Peskov⁵³, Y. Pestov⁵, V. Petráček⁴⁰, V. Petrov¹¹², M. Petrovici⁷⁸, C. Petta²⁹, S. Piano¹¹⁰, M. Píkna³⁹, P. Pillot¹¹³, O. Pinazza^{105,36}, L. Pinsky¹²², D.B. Piyarathna¹²², M. Płoskoń⁷⁴, M. Planinic¹²⁹, J. Pluta¹³⁴, S. Pochybova¹³⁶, P.L.M. Podesta-Lerma¹¹⁹, M.G. Poghosyan⁸⁶, B. Polichtchouk¹¹², N. Poljak¹²⁹, W. Poonsawat¹¹⁴, A. Pop⁷⁸, S. Porteboeuf-Houssais⁷⁰, J. Porter⁷⁴, J. Pospisil⁸³, S.K. Prasad⁴, R. Preghenella^{105,36}, F. Prino¹¹¹, C.A. Pruneau¹³⁵, I. Pshenichnov⁵⁶, M. Puccio¹¹¹, G. Puddu²⁵, P. Pujahari¹³⁵, V. Punin⁹⁹, J. Putschke¹³⁵, H. Qvigstad²², A. Rachevski¹¹⁰, S. Raha⁴, S. Rajput⁹⁰, J. Rak¹²³, A. Rakotozafindrabe¹⁵, L. Ramello³², R. Raniwala⁹¹, S. Raniwala⁹¹, S.S. Räsänen⁴⁶, B.T. Rascanu⁵³, D. Rathee⁸⁷, K.F. Read¹²⁵, J.S. Real⁷¹, K. Redlich⁷⁷, R.J. Reed¹³⁵, A. Rehman¹⁸, P. Reichelt⁵³, F. Reidt^{93,36}, X. Ren⁷, R. Renfordt⁵³, A.R. Reolon⁷², A. Reshetin⁵⁶, F. Rettig⁴³, J.-P. Revol¹², K. Reygers⁹³, V. Riabov⁸⁵, R.A. Ricci⁷³, T. Richert³⁴, M. Richter²², P. Riedler³⁶, W. Riegler³⁶, F. Rigg²⁹, C. Ristea⁶², A. Rivetti¹¹¹, E. Rocco⁵⁷, M. Rodríguez Cahuantzi², A. Rodriguez Manso⁸¹, K. Røed²², E. Rogochaya⁶⁶, D. Rohr⁴³, D. Röhrich¹⁸, R. Romita¹²⁴, F. Ronchetti⁷², L. Ronflette¹¹³, P. Rosnet⁷⁰, A. Rossi^{30,36}, F. Roukoutakis⁸⁸, A. Roy⁴⁹, C. Roy⁵⁵, P. Roy¹⁰¹, A.J. Rubio Montero¹⁰, R. Rui²⁶, R. Russo²⁷, E. Ryabinkin¹⁰⁰, Y. Ryabov⁸⁵, A. Rybicki¹¹⁷, S. Sadovsky¹¹², K. Šafařík³⁶, B. Sahlmuller⁵³, P. Sahoo⁴⁹, R. Sahoo⁴⁹, S. Sahoo⁶¹, P.K. Sahu⁶¹, J. Saini¹³², S. Sakai⁷², M.A. Saleh¹³⁵,

C.A. Salgado¹⁷, J. Salzwedel²⁰, S. Sambyal⁹⁰, V. Samsonov⁸⁵, X. Sanchez Castro⁵⁵, L. Šándor⁵⁹,
 A. Sandoval⁶⁴, M. Sano¹²⁸, D. Sarkar¹³², E. Scapparone¹⁰⁵, F. Scarlassara³⁰, R.P. Scharenberg⁹⁵,
 C. Schiaua⁷⁸, R. Schicker⁹³, C. Schmidt⁹⁷, H.R. Schmidt³⁵, S. Schuchmann⁵³, J. Schukraft³⁶, M. Schulc⁴⁰,
 T. Schuster¹³⁷, Y. Schutz^{113,36}, K. Schwarz⁹⁷, K. Schweda⁹⁷, G. Sciol²⁸, E. Scomparin¹¹¹, R. Scott¹²⁵,
 K.S. Seeder¹²⁰, J.E. Seger⁸⁶, Y. Sekiguchi¹²⁷, D. Sekihata⁴⁷, I. Selyuzhenkov⁹⁷, K. Senosi⁶⁵, J. Seo^{96,67},
 E. Serradilla^{64,10}, A. Sevcenco⁶², A. Shabanov⁵⁶, A. Shabetai¹¹³, O. Shadura³, R. Shahoyan³⁶,
 A. Shangaraev¹¹², A. Sharma⁹⁰, M. Sharma⁹⁰, M. Sharma⁹⁰, N. Sharma^{125,61}, K. Shigaki⁴⁷, K. Shtejer^{9,27},
 Y. Sibiriak¹⁰⁰, S. Siddhanta¹⁰⁶, K.M. Sielewicz³⁶, T. Siemianczuk⁷⁷, D. Silvermyr^{84,34}, C. Silvestre⁷¹,
 G. Simatovic¹²⁹, G. Simonetti³⁶, R. Singaraju¹³², R. Singh⁷⁹, S. Singha^{132,79}, V. Singhal¹³², B.C. Sinha¹³²,
 T. Sinha¹⁰¹, B. Sitar³⁹, M. Sitta³², T.B. Skaali²², M. Slupecki¹²³, N. Smirnov¹³⁷, R.J.M. Snellings⁵⁷,
 T.W. Snellman¹²³, C. Søgaard³⁴, R. Soltz⁷⁵, J. Song⁹⁶, M. Song¹³⁸, Z. Song⁷, F. Soramel³⁰, S. Sorensen¹²⁵,
 M. Spacek⁴⁰, E. Spiriti⁷², I. Sputowska¹¹⁷, M. Spyropoulou-Stassinaki⁸⁸, B.K. Srivastava⁹⁵, J. Stachel⁹³,
 I. Stan⁶², G. Stefanek⁷⁷, M. Steinpreis²⁰, E. Stenlund³⁴, G. Steyn⁶⁵, J.H. Stiller⁹³, D. Stocco¹¹³, P. Strmen³⁹,
 A.A.P. Suaide¹²⁰, T. Sugitate⁴⁷, C. Suire⁵¹, M. Suleymanov¹⁶, R. Sultanov⁵⁸, M. Šumbera⁸³,
 T.J.M. Symons⁷⁴, A. Szabo³⁹, A. Szanto de Toledo^{120,i}, I. Szarka³⁹, A. Szczepankiewicz³⁶, M. Szymanski¹³⁴,
 J. Takahashi¹²¹, N. Tanaka¹²⁸, M.A. Tangaro³³, J.D. Tapia Takaki^{iii,51}, A. Tarantola Peloni⁵³, M. Tarhini⁵¹,
 M. Tariq¹⁹, M.G. Tarzila⁷⁸, A. Tauro³⁶, G. Tejeda Muñoz², A. Telesca³⁶, K. Terasaki¹²⁷, C. Terrevoli^{30,25},
 B. Teyssier¹³⁰, J. Thäder^{74,97}, D. Thomas¹¹⁸, R. Tieulent¹³⁰, A.R. Timmins¹²², A. Toia⁵³, S. Trogolo¹¹¹,
 V. Trubnikov³, W.H. Trzaska¹²³, T. Tsuji¹²⁷, A. Tumkin⁹⁹, R. Turrisi¹⁰⁸, T.S. Tveter²², K. Ullaland¹⁸,
 A. Uras¹³⁰, G.L. Usai²⁵, A. Utrobicic¹²⁹, M. Vajzer⁸³, M. Vala⁵⁹, L. Valencia Palomo⁷⁰, S. Vallero²⁷, J. Van
 Der Maarel⁵⁷, J.W. Van Hoorn³⁶, M. van Leeuwen⁵⁷, T. Vanat⁸³, P. Vande Vyvre³⁶, D. Varga¹³⁶, A. Vargas²,
 M. Vargyas¹²³, R. Varma⁴⁸, M. Vasileiou⁸⁸, A. Vasiliev¹⁰⁰, A. Vauthier⁷¹, V. Vechernin¹³¹, A.M. Veen⁵⁷,
 M. Veldhoen⁵⁷, A. Velure¹⁸, M. Venaruzzo⁷³, E. Vercellin²⁷, S. Vergara Limón², R. Vernet⁸, M. Verweij^{135,36},
 L. Vickovic¹¹⁶, G. Viesti^{30,i}, J. Viinikainen¹²³, Z. Vilakazi¹²⁶, O. Villalobos Baillie¹⁰², A. Vinogradov¹⁰⁰,
 L. Vinogradov¹³¹, Y. Vinogradov^{99,i}, T. Virgili³¹, V. Vislavicius³⁴, Y.P. Viyogi¹³², A. Vodopyanov⁶⁶,
 M.A. Völkl⁹³, K. Voloshin⁵⁸, S.A. Voloshin¹³⁵, G. Volpe^{136,36}, B. von Haller³⁶, I. Vorobyev^{37,92},
 D. Vranic^{36,97}, J. Vrláková⁴¹, B. Vulpescu⁷⁰, A. Vyushin⁹⁹, B. Wagner¹⁸, J. Wagner⁹⁷, H. Wang⁵⁷,
 M. Wang^{7,113}, Y. Wang⁹³, D. Watanabe¹²⁸, Y. Watanabe¹²⁷, M. Weber³⁶, S.G. Weber⁹⁷, J.P. Wessels⁵⁴,
 U. Westerhoff⁵⁴, J. Wiechula³⁵, J. Wikne²², M. Wilde⁵⁴, G. Wilk⁷⁷, J. Wilkinson⁹³, M.C.S. Williams¹⁰⁵,
 B. Windelband⁹³, M. Winn⁹³, C.G. Yaldo¹³⁵, H. Yang⁵⁷, P. Yang⁷, S. Yano⁴⁷, Z. Yin⁷, H. Yokoyama¹²⁸,
 I.-K. Yoo⁹⁶, V. Yurchenko³, I. Yushmanov¹⁰⁰, A. Zaborowska¹³⁴, V. Zaccolo⁸⁰, A. Zaman¹⁶, C. Zampolli¹⁰⁵,
 H.J.C. Zanolli¹²⁰, S. Zaporozhets⁶⁶, N. Zardoshti¹⁰², A. Zarochentsev¹³¹, P. Závada⁶⁰, N. Zaviyalov⁹⁹,
 H. Zbroszczyk¹³⁴, I.S. Zgura⁶², M. Zhalov⁸⁵, H. Zhang^{18,7}, X. Zhang⁷⁴, Y. Zhang⁷, C. Zhao²²,
 N. Zhigareva⁵⁸, D. Zhou⁷, Y. Zhou^{80,57}, Z. Zhou¹⁸, H. Zhu^{18,7}, J. Zhu^{113,7}, X. Zhu⁷, A. Zichichi^{12,28},
 A. Zimmermann⁹³, M.B. Zimmermann^{54,36}, G. Zinovjev³, M. Zyzak⁴³

Affiliation notes

ⁱ Deceased

ⁱⁱ Also at: M.V. Lomonosov Moscow State University, D.V. Skobeltsyn Institute of Nuclear, Physics, Moscow, Russia

ⁱⁱⁱ Also at: University of Kansas, Lawrence, Kansas, United States

Collaboration Institutes

¹ A.I. Alikhanyan National Science Laboratory (Yerevan Physics Institute) Foundation, Yerevan, Armenia

² Benemérita Universidad Autónoma de Puebla, Puebla, Mexico

³ Bogolyubov Institute for Theoretical Physics, Kiev, Ukraine

⁴ Bose Institute, Department of Physics and Centre for Astroparticle Physics and Space Science (CAPSS), Kolkata, India

⁵ Budker Institute for Nuclear Physics, Novosibirsk, Russia

⁶ California Polytechnic State University, San Luis Obispo, California, United States

⁷ Central China Normal University, Wuhan, China

⁸ Centre de Calcul de l'IN2P3, Villeurbanne, France

⁹ Centro de Aplicaciones Tecnológicas y Desarrollo Nuclear (CEADEN), Havana, Cuba

¹⁰ Centro de Investigaciones Energéticas Medioambientales y Tecnológicas (CIEMAT), Madrid, Spain

¹¹ Centro de Investigación y de Estudios Avanzados (CINVESTAV), Mexico City and Mérida, Mexico

¹² Centro Fermi - Museo Storico della Fisica e Centro Studi e Ricerche “Enrico Fermi”, Rome, Italy
¹³ Chicago State University, Chicago, Illinois, USA
¹⁴ China Institute of Atomic Energy, Beijing, China
¹⁵ Commissariat à l’Energie Atomique, IRFU, Saclay, France
¹⁶ COMSATS Institute of Information Technology (CIIT), Islamabad, Pakistan
¹⁷ Departamento de Física de Partículas and IGFAE, Universidad de Santiago de Compostela, Santiago de Compostela, Spain
¹⁸ Department of Physics and Technology, University of Bergen, Bergen, Norway
¹⁹ Department of Physics, Aligarh Muslim University, Aligarh, India
²⁰ Department of Physics, Ohio State University, Columbus, Ohio, United States
²¹ Department of Physics, Sejong University, Seoul, South Korea
²² Department of Physics, University of Oslo, Oslo, Norway
²³ Dipartimento di Elettrotecnica ed Elettronica del Politecnico, Bari, Italy
²⁴ Dipartimento di Fisica dell’Università ‘La Sapienza’ and Sezione INFN Rome, Italy
²⁵ Dipartimento di Fisica dell’Università and Sezione INFN, Cagliari, Italy
²⁶ Dipartimento di Fisica dell’Università and Sezione INFN, Trieste, Italy
²⁷ Dipartimento di Fisica dell’Università and Sezione INFN, Turin, Italy
²⁸ Dipartimento di Fisica e Astronomia dell’Università and Sezione INFN, Bologna, Italy
²⁹ Dipartimento di Fisica e Astronomia dell’Università and Sezione INFN, Catania, Italy
³⁰ Dipartimento di Fisica e Astronomia dell’Università and Sezione INFN, Padova, Italy
³¹ Dipartimento di Fisica ‘E.R. Caianiello’ dell’Università and Gruppo Collegato INFN, Salerno, Italy
³² Dipartimento di Scienze e Innovazione Tecnologica dell’Università del Piemonte Orientale and Gruppo Collegato INFN, Alessandria, Italy
³³ Dipartimento Interateneo di Fisica ‘M. Merlin’ and Sezione INFN, Bari, Italy
³⁴ Division of Experimental High Energy Physics, University of Lund, Lund, Sweden
³⁵ Eberhard Karls Universität Tübingen, Tübingen, Germany
³⁶ European Organization for Nuclear Research (CERN), Geneva, Switzerland
³⁷ Excellence Cluster Universe, Technische Universität München, Munich, Germany
³⁸ Faculty of Engineering, Bergen University College, Bergen, Norway
³⁹ Faculty of Mathematics, Physics and Informatics, Comenius University, Bratislava, Slovakia
⁴⁰ Faculty of Nuclear Sciences and Physical Engineering, Czech Technical University in Prague, Prague, Czech Republic
⁴¹ Faculty of Science, P.J. Šafárik University, Košice, Slovakia
⁴² Faculty of Technology, Buskerud and Vestfold University College, Vestfold, Norway
⁴³ Frankfurt Institute for Advanced Studies, Johann Wolfgang Goethe-Universität Frankfurt, Frankfurt, Germany
⁴⁴ Gangneung-Wonju National University, Gangneung, South Korea
⁴⁵ Gauhati University, Department of Physics, Guwahati, India
⁴⁶ Helsinki Institute of Physics (HIP), Helsinki, Finland
⁴⁷ Hiroshima University, Hiroshima, Japan
⁴⁸ Indian Institute of Technology Bombay (IIT), Mumbai, India
⁴⁹ Indian Institute of Technology Indore, Indore (IITI), India
⁵⁰ Inha University, Incheon, South Korea
⁵¹ Institut de Physique Nucléaire d’Orsay (IPNO), Université Paris-Sud, CNRS-IN2P3, Orsay, France
⁵² Institut für Informatik, Johann Wolfgang Goethe-Universität Frankfurt, Frankfurt, Germany
⁵³ Institut für Kernphysik, Johann Wolfgang Goethe-Universität Frankfurt, Frankfurt, Germany
⁵⁴ Institut für Kernphysik, Westfälische Wilhelms-Universität Münster, Münster, Germany
⁵⁵ Institut Pluridisciplinaire Hubert Curien (IPHC), Université de Strasbourg, CNRS-IN2P3, Strasbourg, France
⁵⁶ Institute for Nuclear Research, Academy of Sciences, Moscow, Russia
⁵⁷ Institute for Subatomic Physics of Utrecht University, Utrecht, Netherlands
⁵⁸ Institute for Theoretical and Experimental Physics, Moscow, Russia
⁵⁹ Institute of Experimental Physics, Slovak Academy of Sciences, Košice, Slovakia
⁶⁰ Institute of Physics, Academy of Sciences of the Czech Republic, Prague, Czech Republic
⁶¹ Institute of Physics, Bhubaneswar, India
⁶² Institute of Space Science (ISS), Bucharest, Romania

⁶³ Instituto de Ciencias Nucleares, Universidad Nacional Autónoma de México, Mexico City, Mexico
⁶⁴ Instituto de Física, Universidad Nacional Autónoma de México, Mexico City, Mexico
⁶⁵ iThemba LABS, National Research Foundation, Somerset West, South Africa
⁶⁶ Joint Institute for Nuclear Research (JINR), Dubna, Russia
⁶⁷ Konkuk University, Seoul, South Korea
⁶⁸ Korea Institute of Science and Technology Information, Daejeon, South Korea
⁶⁹ KTO Karatay University, Konya, Turkey
⁷⁰ Laboratoire de Physique Corpusculaire (LPC), Clermont Université, Université Blaise Pascal, CNRS-IN2P3, Clermont-Ferrand, France
⁷¹ Laboratoire de Physique Subatomique et de Cosmologie, Université Grenoble-Alpes, CNRS-IN2P3, Grenoble, France
⁷² Laboratori Nazionali di Frascati, INFN, Frascati, Italy
⁷³ Laboratori Nazionali di Legnaro, INFN, Legnaro, Italy
⁷⁴ Lawrence Berkeley National Laboratory, Berkeley, California, United States
⁷⁵ Lawrence Livermore National Laboratory, Livermore, California, United States
⁷⁶ Moscow Engineering Physics Institute, Moscow, Russia
⁷⁷ National Centre for Nuclear Studies, Warsaw, Poland
⁷⁸ National Institute for Physics and Nuclear Engineering, Bucharest, Romania
⁷⁹ National Institute of Science Education and Research, Bhubaneswar, India
⁸⁰ Niels Bohr Institute, University of Copenhagen, Copenhagen, Denmark
⁸¹ Nikhef, Nationaal instituut voor subatomaire fysica, Amsterdam, Netherlands
⁸² Nuclear Physics Group, STFC Daresbury Laboratory, Daresbury, United Kingdom
⁸³ Nuclear Physics Institute, Academy of Sciences of the Czech Republic, Řež u Prahy, Czech Republic
⁸⁴ Oak Ridge National Laboratory, Oak Ridge, Tennessee, United States
⁸⁵ Petersburg Nuclear Physics Institute, Gatchina, Russia
⁸⁶ Physics Department, Creighton University, Omaha, Nebraska, United States
⁸⁷ Physics Department, Panjab University, Chandigarh, India
⁸⁸ Physics Department, University of Athens, Athens, Greece
⁸⁹ Physics Department, University of Cape Town, Cape Town, South Africa
⁹⁰ Physics Department, University of Jammu, Jammu, India
⁹¹ Physics Department, University of Rajasthan, Jaipur, India
⁹² Physik Department, Technische Universität München, Munich, Germany
⁹³ Physikalisches Institut, Ruprecht-Karls-Universität Heidelberg, Heidelberg, Germany
⁹⁴ Politecnico di Torino, Turin, Italy
⁹⁵ Purdue University, West Lafayette, Indiana, United States
⁹⁶ Pusan National University, Pusan, South Korea
⁹⁷ Research Division and ExtreMe Matter Institute EMMI, GSI Helmholtzzentrum für Schwerionenforschung, Darmstadt, Germany
⁹⁸ Rudjer Bošković Institute, Zagreb, Croatia
⁹⁹ Russian Federal Nuclear Center (VNIIEF), Sarov, Russia
¹⁰⁰ Russian Research Centre Kurchatov Institute, Moscow, Russia
¹⁰¹ Saha Institute of Nuclear Physics, Kolkata, India
¹⁰² School of Physics and Astronomy, University of Birmingham, Birmingham, United Kingdom
¹⁰³ Sección Física, Departamento de Ciencias, Pontificia Universidad Católica del Perú, Lima, Peru
¹⁰⁴ Sezione INFN, Bari, Italy
¹⁰⁵ Sezione INFN, Bologna, Italy
¹⁰⁶ Sezione INFN, Cagliari, Italy
¹⁰⁷ Sezione INFN, Catania, Italy
¹⁰⁸ Sezione INFN, Padova, Italy
¹⁰⁹ Sezione INFN, Rome, Italy
¹¹⁰ Sezione INFN, Trieste, Italy
¹¹¹ Sezione INFN, Turin, Italy
¹¹² SSC IHEP of NRC Kurchatov institute, Protvino, Russia
¹¹³ SUBATECH, Ecole des Mines de Nantes, Université de Nantes, CNRS-IN2P3, Nantes, France
¹¹⁴ Suranaree University of Technology, Nakhon Ratchasima, Thailand
¹¹⁵ Technical University of Košice, Košice, Slovakia

¹¹⁶ Technical University of Split FESB, Split, Croatia
¹¹⁷ The Henryk Niewodniczanski Institute of Nuclear Physics, Polish Academy of Sciences, Cracow, Poland
¹¹⁸ The University of Texas at Austin, Physics Department, Austin, Texas, USA
¹¹⁹ Universidad Autónoma de Sinaloa, Culiacán, Mexico
¹²⁰ Universidade de São Paulo (USP), São Paulo, Brazil
¹²¹ Universidade Estadual de Campinas (UNICAMP), Campinas, Brazil
¹²² University of Houston, Houston, Texas, United States
¹²³ University of Jyväskylä, Jyväskylä, Finland
¹²⁴ University of Liverpool, Liverpool, United Kingdom
¹²⁵ University of Tennessee, Knoxville, Tennessee, United States
¹²⁶ University of the Witwatersrand, Johannesburg, South Africa
¹²⁷ University of Tokyo, Tokyo, Japan
¹²⁸ University of Tsukuba, Tsukuba, Japan
¹²⁹ University of Zagreb, Zagreb, Croatia
¹³⁰ Université de Lyon, Université Lyon 1, CNRS/IN2P3, IPN-Lyon, Villeurbanne, France
¹³¹ V. Fock Institute for Physics, St. Petersburg State University, St. Petersburg, Russia
¹³² Variable Energy Cyclotron Centre, Kolkata, India
¹³³ Vinča Institute of Nuclear Sciences, Belgrade, Serbia
¹³⁴ Warsaw University of Technology, Warsaw, Poland
¹³⁵ Wayne State University, Detroit, Michigan, United States
¹³⁶ Wigner Research Centre for Physics, Hungarian Academy of Sciences, Budapest, Hungary
¹³⁷ Yale University, New Haven, Connecticut, United States
¹³⁸ Yonsei University, Seoul, South Korea
¹³⁹ Zentrum für Technologietransfer und Telekommunikation (ZTT), Fachhochschule Worms, Worms, Germany